UNIVERSITY OF COPENHAGEN
FACULTY OF SCIENCE

DAWN

Master's thesis

Finding the most efficient survey design for discovering high-redshift galaxies with *JWST*

Author: Luka Vujeva
Advisor: Charles L. Steinhardt
Date: 22 May 2023

Institute:	Cosmic Dawn Center (DAWN), Niels Bohr Institute
Author(s):	Luka Vujeva
Title :	Finding the most efficient survey design for discovering high-redshift galaxies with *JWST*
Description:	The goal of this project is to determine the most efficient survey strategy for finding ultra-high redshift galaxies using the James Webb Space Telescope.
Advisor:	Charles L. Steinhardt
Date:	22 / 5 / 2023
Cover Photo:	Abell 370, BUFFALO collaboration (Steinhardt et al., 2020)

Table of content

Abstract

The James Webb Space Telescope (*JWST*) is the first telescope capable of probing the creation of the earliest galaxies in the Universe. Several large blank field observing programs aimed at combating the effects of cosmic variance at high redshifts such as JADES and CEERS have been unsuccessful in probing the critical $15 \leq z \leq 20$ regime in which the first galaxies are believed to have formed. This has motivated the search for a survey strategy that will be able to effectively probe this redshift regime. This work analyzes the use of gravitationally lensed fields, which has historically been the most effective discovery tool with the Hubble Space Telescope (*HST*), utilizing the 6 galaxy clusters which provided the highest median magnification factor within a single *JWST* NIRCam pointing (2.1'x2.1') in order to suppress the effects of cosmic variance at high redshift. Testing was conducted using the magnification maps of archival models of the 6 clusters selected from the CLASH/MUSES catalogues, modelled using both *HST* and *JWST* data, and simulated massive elliptical galaxies created using `LENSTOOL`. The lens models were used in combination with mock survey code which employs the use of a luminosity function extrapolated into the $z > 8$ regime in conjunction with a cosmic variance calculator `cosmic-variance` in order to estimate both the expected number of galaxies as a function of redshift and the highest redshift galaxy one would expect to see in a given survey strategy. These results were then compared against the results of large area, blank field surveys such as JADES and CEERS in order to determine the most effective survey strategy for *JWST*. We found that the fields containing massive foreground galaxy clusters specifically chosen to have the highest median magnification factor within the NIRCam pointing provide the highest probability of both probing the $15 \leq z \leq 20$ regime, as well as discovering the highest redshift galaxy possible with *JWST*. Such a survey strategy would also be significantly more time effective given the fewer lines of sight required to discover these ultra-high redshift galaxies.

1 Introduction

JWST is the first telescope that will be able to observe galaxies in their initial state of assembly, rather than their subsequent evolution. Although we do not have direct observational constraints on galaxy assembly, the formation of halos that will host galaxies is robustly predicted both analytically and numerically. These models predict that the first galaxies should only appear between redshifts of $15 \leq z \leq 20$ (Yung et al., 2023; Lacey et al., 2011; Bromm & Yoshida, 2011; Springel et al., 2005). This means that *JWST* should be capable of finding this first generation of galaxies. Pinpointing the timing of this first generation will also provide a test of different halo assembly models, along with models predicting the age of the Universe at which the first stars formed. Additionally, it will allow us to pinpoint the beginning of the cosmic ”dark ages”, in which neutral hydrogen obscures the light from the first galaxies, thus preventing us from directly observing them.

However, finding such galaxies requires an optimized search strategy. The early success of *JWST* has allowed us to observe a new regime of high-redshift galaxies in blank fields, which have been spectroscopically confirmed to lie at redshifts of up to $z = 13.2$ (Robertson et al., 2022). This is rapidly approaching the predicted redshift regime for the birth of the first galaxies in the Universe, however we have yet to directly observe the beginning of the dark ages. Therefore, the current limit of *JWST* does not fall within the dark ages of the Universe.

This limit will be further constrained as we update our halo mass functions using the newly discovered high-redshift galaxies found by *JWST*. In the blank fields in which these galaxies have been found, it is statistically unlikely to find a galaxy at a redshift $z \geq 14$, thus not allowing us to probe the limiting redshift of the cosmic dark ages. However, we have not employed optimized search strategies to probe the $15 \leq z \leq 20$ regime which *JWST* should be capable of probing. The method this work presents uses the galaxy clusters that provide the highest median magnification factor within a single NIRCam pointing in order to give us the highest probability of finding a galaxy within the uncertain limits of the highest redshift at which we should be able to see a galaxy.

1.1 History of Gravitational Lensing

Gravitational lensing occurs when the gravitational potential of a massive object such as a large galaxy or a massive cluster of galaxies bends its surrounding space-time and allows for the light coming from a background source to be deflected along the path to the observer.

The first arguments for light's path being bent around a massive object came out of Isaac Newton's 1704 book *Opticks* (Newton, 1704). In 1801, Johann Georg von Soldner calculated the deflection angle of light travelling past a massive object using Newton's findings, and found that for light coming from a point source moving through a spherically symmetric gravitational field, the deflection angle is

$$\hat{\alpha} = \frac{2GM}{c^2 b} \, , \tag{1}$$

where G is the gravitational constant, c is the speed of light in a vacuum, M is the mass of the foreground lens, and b is the impact parameter of the light coming from the original source. A sketch of this can be seen in Fig. 3.

Von Soldner originally computed this relationship for the case in which the gravitational potential of the Sun would be deflecting the light coming from background stars. By setting $M = M_\odot \approx 1.989 \times 10^{30}$ kg, and since they would be searching for light being bent around the edges of the sun, $b \approx R_\odot \approx 6.96 \times 10^8$ m. This resulted in a deflection angle of 0.875".

In 1915, Einstein published his theory of General Relativity, which generalized special relativity and related the curvature of space-time to the energy and momentum of the object. A key result of this theory is that for a photon travelling along a null geodesic, its deflection angle when passing through a spherically symmetrical gravitational potential is

$$\hat{\alpha} = \frac{4GM}{c^2 b} \, . \tag{2}$$

This is exactly two times greater than the value computed from Newtonian gravity by von Soldner. In order to test this tension, in 1919, Arthur Eddington and Frank

Watson Dyson took detailed images of a total solar eclipse, which would allow for the stars near the sun to be more easily observed. The goal of the observations was simple: measure the deflection angle of the light coming from the stars near the surface of the sun using the known positions of other reference stars nearby.

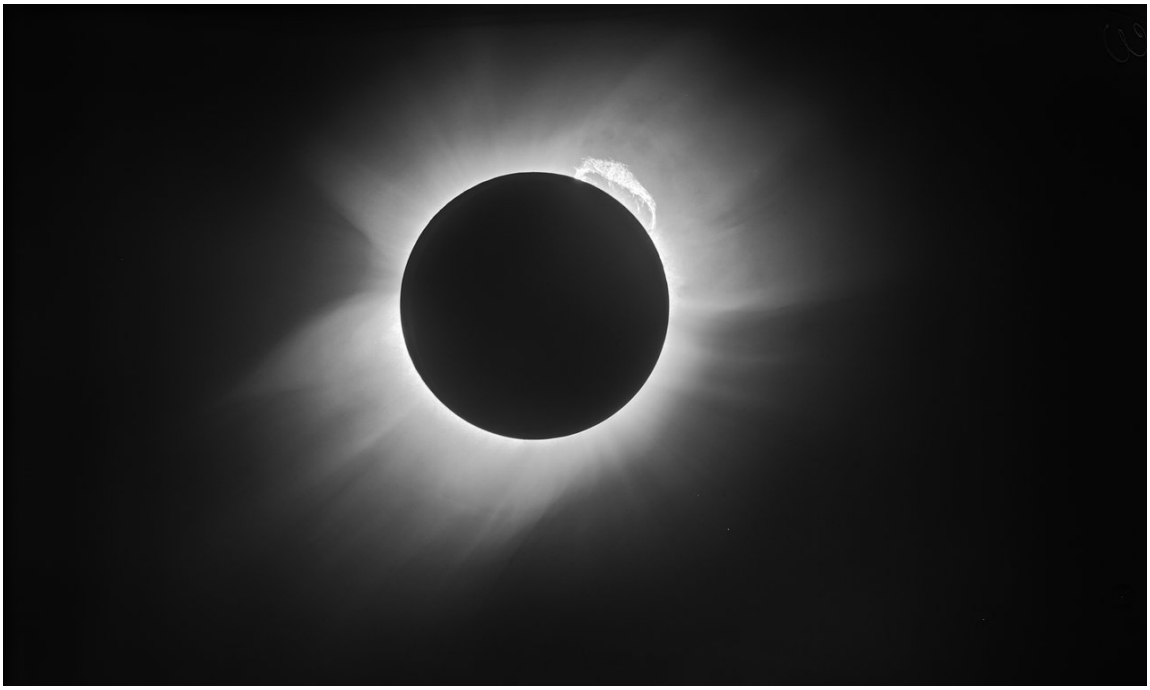

Figure 1: Image of the May 29th 1919 solar eclipse that was used to compare the relative locations of known stars in order to test Einstein's theory of General Relativity. This image was originally taken from Eddington's 1919 paper (Dyson et al., 1920), however this is a modern processed image of the original photographic plate. Credit: ESO/Landessternwarte Heidelberg-Königstuhl/F. W. Dyson, A. S. Eddington, & C. Davidson

1.2 Dark Matter Halos

A critical step towards accurately modelling gravitational lenses caused by galaxies and galaxy clusters is understanding the way that dark matter assembles into halos. These halos are present in both galaxies and galaxy clusters, and account

for more than 10 times the mass of the visible baryonic matter (White et al., 1993; White & Fabian, 1995; Lubin et al., 1996). This means that most of the effects of gravitational lensing that we are seeing are caused by the electromagnetically invisible dark matter in these structures, not by the baryonic matter.

The most visually striking case of this discrepancy comes from observations of the Bullet Cluster, which is a galaxy cluster located at a redshift of $z = 0.296$, and is a prime example of two smaller clusters in the process of merging.

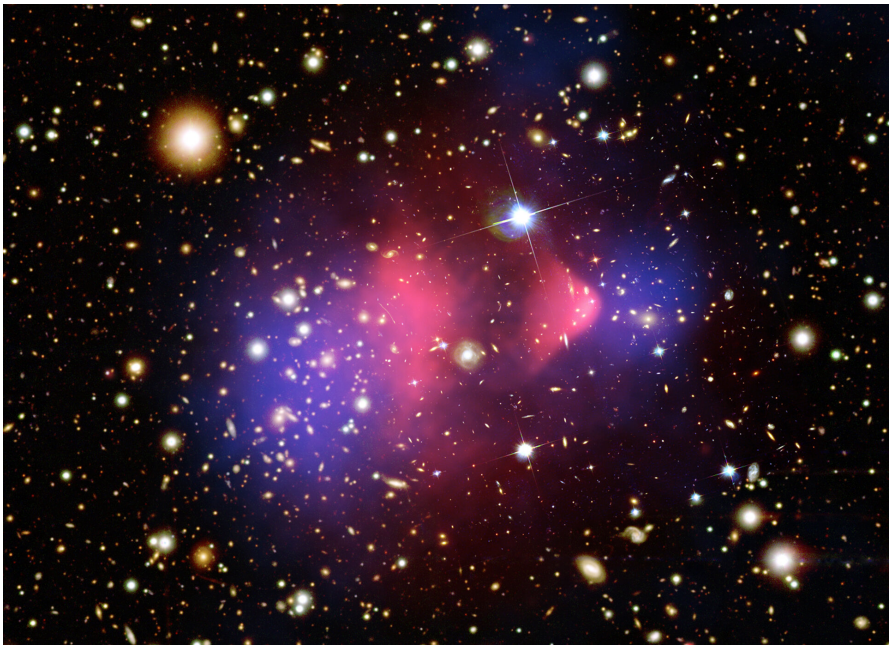

Figure 2: Composite image of the Bullet Cluster, imaged by the Magellan and Hubble telescopes, with X-ray emission captured by the Chandra telescope shown in pink. The blue glow is the dark matter distribution estimated using gravitational lensing maps (Clowe et al., 2006). Credit: X-ray: NASA/CXC/CfA/M.Markevitch, Optical and lensing map: NASA/STScI, Magellan/U.Arizona/D.Clowe, Lensing map: ESO WFI

Fig.2 shows that the center of the dark matter distribution (shown in blue) is significantly offset from the center of the baryonic matter distribution (shown in pink) in the cluster. The dark matter is inferred from the gravitational lens model generated for the cluster, which is built by assuming a density distribution (such as the NFW

profile discussed in Sec. 2.1), and then using the locations and luminosities of the multiple images of the background galaxies to constrain both the shape of the dark matter halo, as well as its mass and concentration. The mass of the Bullet Cluster contained within a 500 kpc radius from the center of the cluster was estimated at $M_{r=500\ kpc} = 5.3 \times 10^{14} M_{\odot}$ (Clowe et al., 2004). Clowe et al. (2006) concluded that the 8σ difference between the central peaks of the total mass and the baryonic mass can only be explained by the presence of dark matter, and that the majority of the mass in the cluster comes from the dark matter components. The discrepancy between the locations of the dark matter and ionized plasma comes from the fact that in cluster mergers, galaxies act like collisionless particles (Clowe et al., 2006), whereas the pink intracluster medium (ICM) experiences ram pressure, which results in the decoupling of the two components.

2 Gravitational Lensing Formalism

This section outlines the formalism associated with describing the density distribution of dark matter halos, as well as the equations necessary to describe the lensing effects cuased by them.

2.1 The NFW Profile

One of the main challenges in modelling dark matter halos is that we cannot directly measure their density distribution. This means that we must rely on theoretical models of dark matter halos in order to build our lens models.

The simplest form that a dark matter halo could take is an isothermal sphere, where the density distribution of the dark matter halo would evolve with radius as

$$\rho(r) \propto r^{-2} \ \texttt{for} \ \ r \leq r_h \ , \tag{3}$$

where r_h is the radius at which the mean density contained within the radius is

$$\rho_h = \Delta_h \overline{\rho} = \Delta_h \rho_{cr} \Omega_m \ , \tag{4}$$

where $\overline{\rho}$ is the mean matter density of the Universe at a given time t, ρ_{cr} is the critical density of the Universe at that same time, and Δ_h describes the over-density of the region. In practice, the most common choices for this over-density parameter are either $\Delta_h = \Delta_{vir}$, or more commonly when describing dark matter halos, $\Delta_h = 200$, i.e. where the density is 200 times that of the mean density $\overline{\rho}$.

Although we know that a significant portion of the gas found in galaxies and galaxy clusters takes on an isothermal density distribution, there are multiple key problems with using this density distribution when describing dark matter halos:

1. The outside of the halo might take an infinite amount of time to collapse, which is nonphysical

2. the hierarchical merging of dark matter halos could invalidate the spherical collapse model

Thus, we need to turn to numerical simulations in order to better describe the density distributions of dark matter halos.

In 1996, Navarro, Frenk & White showed that the density profiles of dark matter halos generated in N-body ΛCDM cosmological simulations can be described using a double power law. This allows for the the logarithmic slope at small radii to be ~ -1, and ~ -3 at large radii (Navarro et al., 1997). The resulting "NFW" density profile is described as

$$\rho(r) = \frac{\rho_s}{(r/r_s)(1 + r/r_s)^2} \ , \tag{5}$$

where r_s is the so called scale radius, which is the relationship between the concentration parameter c of the halo, and the radius for a given choice of over-density parameter Δ. For example, given a typical over-density of $\Delta = 200$, $r_s \equiv r_{200}/c$, the scale density ρ_s is simply the product of the critical density of the Universe ρ_{cr} at a time t, and the characteristic over-density parameter δ_c, defined as $\rho_s \equiv \delta_c \rho_{cr}$. The characteristic over-density parameter δ_c is solely dependent on the concentration parameter c for a fixed over-density parameter Δ_h,

$$\delta_c = \frac{\Delta_h}{3} \frac{c^3}{ln(1 + c) - c(1 + c)} \ . \tag{6}$$

The concentration parameter c can tell us a great deal about the formation history of the cluster or galaxy. Halos which formed earlier in cosmic history and have had more time to grow quiescently tend to be more concentrated, where as those that form later on due to large scale merging events tend to have lower concentrations of typically $c \sim 4$ (Zhao et al., 2003; Zhao et al., 2009).

The mass enclosed within this chosen over-density ($\Delta = 200$) can then be expressed as

$$M_{200} = \frac{3}{200} \frac{800\pi}{3} \rho_{cr} r_{200}^3 \ . \tag{7}$$

Follow up studies found that the NFW profile is a suitable representation of equilibrium density profiles for all masses, even those which have undergone hierarchical merging under a ΛCDM cosmology (Navarro et al., 1997).

These results are incredibly powerful given that one can now characterize a dark matter halo using only its mass enclosed in a given over-density M_{Δ}, and its concentration within that over-density c_{Δ}.

2.2 The Lens Equation

Now that we have a robust physical model for the density distribution within a dark matter halo, we can employ it to describe the gravitational lensing caused by such halos.

Below is a sketch of a simple gravitational lens system (Bartelmann & Schneider, 2001).

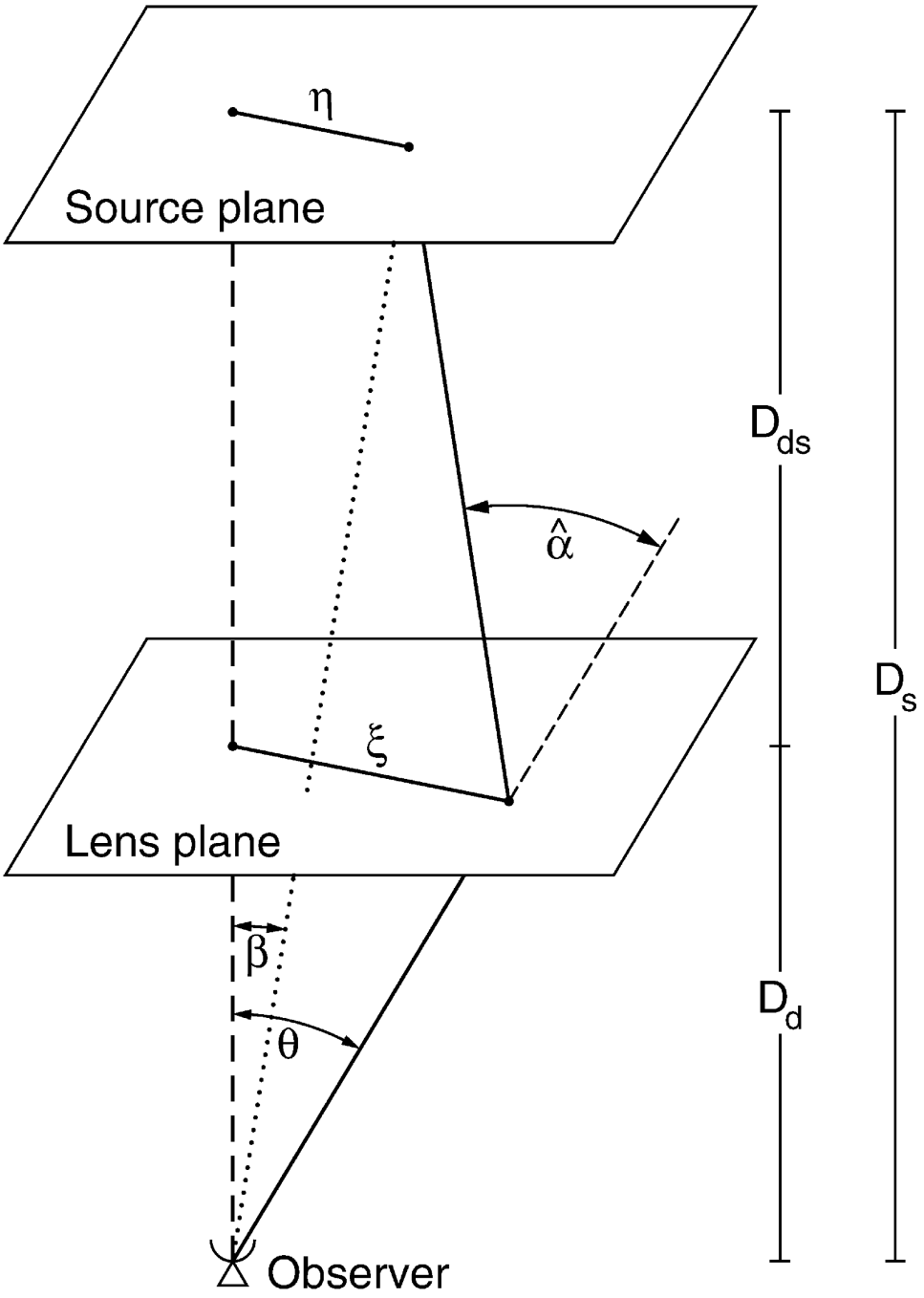

Figure 3: (Reproduced from Fig.11 of Bartelmann & Schneider (2001)) Sketch of a simple gravitational lens system.

The light coming from an object in the source plane will be deflected as it passes through the gravitational potential of the lens in the lens plane. The angle at which the light is deflected is heavily dependent on the location of the object in the source plane, as well as both the strength and geometry of the gravitational potential of the lens.

The locations of the images caused by lensing is determined by the lens equation, which for small α, β, ξ, can be written as

$$\vec{\theta} D_S = \vec{\beta} D_S + \hat{\vec{\alpha}} D_{LS} \ . \tag{8}$$

The reduced deflection angle $\vec{\alpha}(\vec{\theta})$ can be defined as

$$\vec{\alpha}(\vec{\theta}) \equiv \frac{D_{LS}}{D_S} \hat{\vec{\alpha}} \ , \tag{9}$$

which allows us to re-write the lens equation as

$$\vec{\beta} = \vec{\theta} - \vec{\alpha}(\vec{\theta}) \ . \tag{10}$$

From Sec. 1.1, General relativity tells us that the deflection angle of a point mass can be written as

$$\hat{\alpha} = \frac{4GM}{c^2 b} \ . \tag{11}$$

If our impact parameter is expressed as $b = \theta D_L$, then the deflection angle can be re-written as

$$\hat{\alpha} = \frac{4GM}{c^2 \theta D_L} \ , \tag{12}$$

which allows the lens equation to be written as

$$\beta = \theta - \frac{4GM}{c^2 \theta D_L} \frac{D_{LS}}{D_s} \ . \tag{13}$$

This leads us to the definition of the Einstein radius, which is essentially a characteristic scale for the locations of the images caused by the lensing potential (e.g.

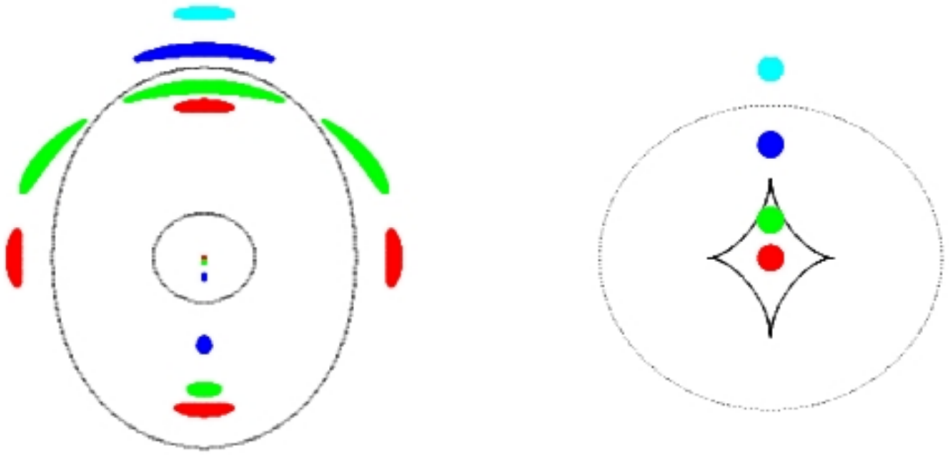

Figure 4: Example of the multiple images created by sources as they move away from the center of an elliptical lens (Narayan & Bartelmann, 1997). The left panel depicts the source plane, where the black lines represent the critical lines, where as the right panel depicts the source plane, where the black lines represent the caustics.

the location of Einstein rings), defined as

$$\theta_E \equiv \sqrt{\frac{4GM}{c^2\theta}\frac{D_{LS}}{D_L D_s}} \, . \tag{14}$$

Therefore, the lens equation can be re-written in terms of the Einstein radius

$$\beta = \theta - \frac{\theta_E^2}{\theta} \, . \tag{15}$$

There are two solutions to this equation, from which the multiple images caused by lensing effects can be seen,

$$\theta_\pm = \frac{1}{2}\left(\beta \pm \sqrt{\beta^2 + 4\theta_E^2}\right) \, . \tag{16}$$

The resulting images fall on either side of the Einstein radius, as seen in Fig. 4.

2.3 The Magnification Factor

Now that we can determine the locations of the images with the lens equation, we can move on to describing the magnification effects of a more realistic gravitational lens, such as a galaxy cluster.

From the Poisson equation, we can write the gravitational potential as

$$\Delta\Phi = 4\pi G\rho \ . \tag{17}$$

If we assume that the dark matter halo of the galaxy cluster follows the Navarro et al. (1997) profile,

$$\rho(r) = \frac{\rho_s}{(r/r_s)(1+r/r_s)^2} \ . \tag{18}$$

Recall from Sec. 2.1 that $\rho_s = \delta_c \rho_{cr}$, where ρ_{cr} is the critical density of the universe at a given redshift,

$$\rho_{cr} = \frac{3H^2(z)}{8\pi G} \ , \tag{19}$$

and δ_c is the characteristic over-density parameter,

$$\delta_c = \frac{200}{3}\frac{c^3}{ln(1+c) - c(1+c)} \ , \tag{20}$$

expressed in terms of the concentration c, which is defined as the ratio between the virial radius r_{200} and the scaled radius r_s, $r_s \equiv r_{200}/c$. The virial radius r_{200} is simply the radius at which the mass density of the dark matter halo is equal to $200\rho_{cr}$. Therefore the mass enclosed within this radius is :

$$M_{200} \equiv \frac{800\pi}{3}\rho_{cr} r_{200}^3 = \frac{800\pi}{3}\frac{\overline{\rho}(z)}{\Omega(z)} r_{200}^3 \ , \tag{21}$$

where M_{200} is the virial mass enclosed by r_{200}.

Next, the surface mass density $\Sigma(x)$ and the critical surface mass density Σ_c will be derived, which will allow us to compute the convergence κ of the NFW profile following the procedure in Wright & Brainerd (1999) using the following relation-

ship:

$$\kappa(x) = \frac{\Sigma(x)}{\Sigma_{cr}} \, , \tag{22}$$

where x is a unitless value that expresses the impact parameter $x \equiv \xi/\xi_0$. An example of $\kappa(x)$ for the cluster CLJ1226.9+3332 can be seen in the upper panel of Fig. 7. $\Sigma(x)$ is the surface mass density of the lens in question, which is directly dependent on x. For an NFW density profile, Wright & Brainerd (1999) found it to be

$$\Sigma_{NFW}(x) = \begin{cases} \frac{2r_s\delta_c\rho_c}{(x^2-1)}\left[1 - \frac{2}{\sqrt{1-x^2}}\,\text{arctanh}\,\sqrt{\frac{1-x}{1+x}}\right] & x < 1 \\ \frac{2r_s\delta_c\rho_c}{3} & x = 1 \\ \frac{2r_s\delta_c\rho_c}{(x^2-1)}\left[1 - \frac{2}{\sqrt{x^2-1}}\,\arctan\,\sqrt{\frac{x-1}{1+x}}\right] & x > 1 \end{cases} . \tag{23}$$

Since the NFW profile is spherically symmetric, we can write the shear parameter $\gamma_{NFW}(x)$, which describes the way that the images are stretched tangentially around the lens (as can be seen in the lower image in Fig. 7), as

$$\gamma_{NFW} = \frac{\overline{\Sigma}_{NFW}(x) - \Sigma_{NFW}(x)}{\Sigma_c} \, , \tag{24}$$

where $\overline{\Sigma}_{NFW}(x)$ is the mean surface mass density as a function of x, given by

$$\overline{\Sigma}_{NFW}(x) = \begin{cases} \frac{4}{x^2}r_s\delta_c\rho_c\left[\frac{2}{\sqrt{1-x^2}}\,\text{arctanh}\,\sqrt{\frac{1-x}{1+x}} + \ln(\frac{x}{2})\right] & x < 1 \\ \frac{2r_s\delta_c\rho_c}{3} & x = 1 \\ \frac{4}{x^2}r_s\delta_c\rho_c\left[\frac{2}{\sqrt{x^2-1}}\,\arctan\,\sqrt{\frac{x-1}{1+x}} + \ln(\frac{x}{2})\right] & x > 1 \end{cases} . \tag{25}$$

This allows us to write the radial dependence of the shear as

$$\gamma_{NFW}(x) = \begin{cases} \frac{r_s \delta_c \rho_c}{\Sigma_c} g_<(x) & x < 1 \\ \frac{r_s \delta_c \rho_c}{\Sigma_c} [\frac{10}{3} + 4 \ln(\frac{1}{2})] & x = 1 \\ \frac{r_s \delta_c \rho_c}{\Sigma_c} g_>(x) & x > 1 \end{cases} , \tag{26}$$

where

$$g_<(x) = \frac{8 \operatorname{arctanh} \sqrt{(1-x)/(1+x)}}{x^2 \sqrt{1-x^2}} + \frac{4}{x^2} \ln(\frac{x}{2}) - \frac{2}{(x^2-1)} + \frac{4 \operatorname{arctanh} \sqrt{(1-x)/(1+x)}}{(x^2-1)(1-x^2)^{1/2}} , \tag{27}$$

$$g_>(x) = \frac{8 \operatorname{arctanh} \sqrt{(x-1)/(1+x)}}{x^2 \sqrt{x^2-1}} + \frac{4}{x^2} \ln(\frac{x}{2}) - \frac{2}{(x^2-1)} + \frac{4 \operatorname{arctan} \sqrt{(x-1)/(1+x)}}{(x^2-1)^{3/2}} . \tag{28}$$

Finally, the critical surface density can be computed as

$$\Sigma_{cr} = \frac{c^2}{4\pi G} \frac{D_S}{D_{LS} D_L} , \tag{29}$$

where in this case, c is the speed of light. It is very important to note that the distance values D_S, D_{LS}, D_L are all angular diameter distances, and not simple linear distance measurements. This means that they cannot be simply added or subtracted. The distances to the lens and to the source were simply computed using the `astropy.cosmology.angular_diameter_distance()` function. However, the distance from the lens to the source $D_{LS} \neq D_S - D_L$. It must be computed using

$$D_{A_{1,2}} = \frac{1}{1+z_2} \left[D_{M_2} \sqrt{1 + \Omega_K (D^2_{M_1}/D^2_H)} - D_{M_1} \sqrt{1 + \Omega_K (D^2_{M_2}/D^2_H)} \right] , \tag{30}$$

Where D_{M_1}, D_{M_2} are the transverse comoving distances to the two objects,

$D_H = 3000\, h^{-1}\, Mpc$ is the Hubble distance, Ω_K is the curvature density parameter, and h is a unitless constant that accounts for our tolerances in the Hubble constant. Here it is taken to be $h = 0.677$. Note that this equation only holds for the cases where $\Omega \geq 0$.

This expression can be simplified by assuming a flat universe, which implies that $\Omega = 0$. This means that our transverse comoving distances D_{M_1}, D_{M_2} now simply become comoving distances D_{C_1}, D_{C_2}, and our equation for angular diameter distance simplifies to

$$D_{A_{1,2}} = \frac{1}{1+z_2}[D_{C_2} - D_{C_1}]\ . \tag{31}$$

We now have all of the necessary tools to compute the convergence $\kappa(x)$ of a cluster with a NFW DM density profile. This allows us to calculate the magnification factor of our cluster as a function of both redshift to the lens z_L, and our unitless impact parameter x.

We can now calculate our magnification parameter μ, which comes from the magnification matrix dependent on the relationship between the shape of the source element of the image in the source plane $d\theta_S$ and the lens plane $d\theta_L$, expressed as

$$\frac{d\vec{\theta}_S}{d\vec{\theta}_L} = A^{-1} = \begin{pmatrix} 1-\kappa+\gamma & 0 \\ 0 & 1-\kappa-\gamma \end{pmatrix} \tag{32}$$

and the magnification factor μ is

$$\mu = det(A) = ((1-\kappa(x))^2 - \gamma_{NFW}(x)^2)^{-1}\ . \tag{33}$$

However, in the case of weak lensing (where we do not see multiple images caused by strong lensing effects), which for example, can be seen in the parallel fields of massive galaxy clusters such as the parallel fields taken of the Hubble Frontier Fields (Johnson et al., 2014), this equation simplifies to

$$\mu = 1 + 2\kappa(x)\ . \tag{34}$$

In the strong lensing case, the magnification factor will be greatest at the critical lines in the lens plane (or the caustics in the source plane). The source's location relative to the caustics will also determine both the number of images seen in the lens plane, as well as the distortion of those images (as illustrated in Fig. 4).

2.4 Lenstool

In order to properly model gravitational lenses, a modelling code such as LENSTOOL (Kneib et al., 1996; Jullo et al., 2007; Jullo & Kneib, 2009) can be employed, which allows users to model the dark matter distribution of a foreground lens by providing it the locations and redshifts of sources that have been multiply imaged by the lens, and then assigning the halo a dark matter distribution. In combination, this allows LENSTOOL to compute the location and shapes of the critical lines and caustics associated with the lens. High-quality photometry is imperative to the success of a model, given that the more multiply imaged sources one can identify, the better constrained the dark matter halo model will be.

In this work, LENSTOOL was used in a slightly non-traditional way. LENSTOOL was employed in order to build synthetic models of galaxy clusters and elliptical galaxies in order to try and identify the ideal combination of mass, lens redshift, and concentration in order to maximize the median magnification factor of a lens within a NIRCam pointing. Instead of feeding LENSTOOL an image of, for example a galaxy cluster, along with the locations and redshifts of a set of multiply imaged sources, it was directly given a dark matter halo mass, lens redshift, concentration, and source redshift. This allows LENSTOOL to directly compute a convergence (κ) and shear (γ) map, scaled for a source at $z = 20$, from which the magnification map could be calculated. An example of one of the models generated by LENSTOOL can be seen in Fig. 9, which corresponds to the magnification map (μ) for an elliptical galaxy of $M_{200} = 10^{13} M_{\odot}, c_{200} = 6, e = 0.25, z_L = 1, z_S = 20$, with an NFW dark matter density profile, shown in the lens plane.

Another key challenge in detecting high-redshift sources is reconstructing the original location and shape of the source in the source plane. LENSTOOL also allows

users to reconstruct the locations and shapes of sources using the deflection maps generated after computing the lens model.

3 Cosmic Variance

A major hindrance to finding high-redshift galaxies is cosmic variance, which is the variance in the number density of galaxies observed within a finite survey volume arising due to the influence of large scale structures on the local number densities of small scale objects.

For N objects, variance is defined as $\langle N^2 \rangle - \langle N \rangle^2$, which is simply the second moment of the probability of counting N objects in a given survey volume V_c. Following Moster et al. (2011), cosmic variance σ_v is defined as

$$\sigma_v^2 = \frac{1}{V^2} \int_V dV_a dV_b \xi(|\mathbf{r_a} - \mathbf{r_b}|) \ , \tag{35}$$

where V is the survey volume, and ξ is the two point correlation function for our survey volume, which simply gives the probability of finding another galaxy within a given distance (Peebles, 1980).

The primary challenge in solving this integral lies within the correlation function, which is not always known. One approach to tackling this problem (and the approach that Moster et al. (2011) takes) is to use estimates of the galaxy bias $b(m_*, z)$ calculated by halo occupation models. The galaxy bias is the statistical relationship between galaxies and their underlying distributions of dark matter (Desjacques et al., 2018), which is a function of both the stellar mass of the galaxies m_*, and redshift z. This allows us to write the galaxy correlation function as

$$\xi = b^2(m_*, z) \xi_{dm}(r, z) \ , \tag{36}$$

and under the assumption that the bias function is scale independent,

$$\begin{aligned}\sigma_v^2 &= \frac{1}{V^2}\int_V dV_a dV_b b^2(m_*,z)\xi_{dm}(r_{ab},z) \\ &= b^2(m_*,z)\frac{1}{V^2}\int_V dV_a dV_b \xi_{dm}(r_{ab},z) \\ &= b^2(m_*,z)\sigma_{dm}^2(z)\ .\end{aligned} \tag{37}$$

The final step is to calculate the cosmic variance for dark matter $\sigma_{dm}^2(z)$, which can be done numerically, with a code such as `QUICKCV` (Newman & Davis, 2002). Thus for a given survey volume, we can now directly compute the cosmic variance as a function of redshift. Fig. 5 shows that cosmic variance increases strongly towards both high mass and high redshift (Sheth et al., 2001; Moster et al., 2011; Steinhardt et al., 2021), meaning that it is significantly harder to discover high mass galaxies in the redshift range in which we are interested within a survey with a small search area.

Although primordial fluctuations produce a small number of extremely over-dense regions which will lead to the quickest gravitational collapse and the first, massive galaxies, these extreme overdensities are tightly clustered, so that most of the first galaxies will appear in a small number of rich fields. That is, the relatively uncommon pointings which have more high-mass, ultra-high redshift galaxies than average are overwhelmingly likely to have more galaxies of any mass at the same redshifts as well. Conversely, the regions containing lower-mass galaxies must still have extreme overdensities in order for their halos to have collapsed so quickly, and thus are very likely to have high-mass galaxies nearby.

Thus, although finding these regions is potentially difficult and may require probing many different sightlines, the discovery of even a single, massive ultra-high redshift galaxy is likely to indicate the presence of many smaller galaxies nearby. Rather than taking photometry deep enough to find galaxies closer to M_* at these redshifts, it is more effective to focus on searching for the high-mass tail of the distribution. This is a far more efficient way of finding which foreground clusters happen to have magnified these uncommon, over-dense regions.

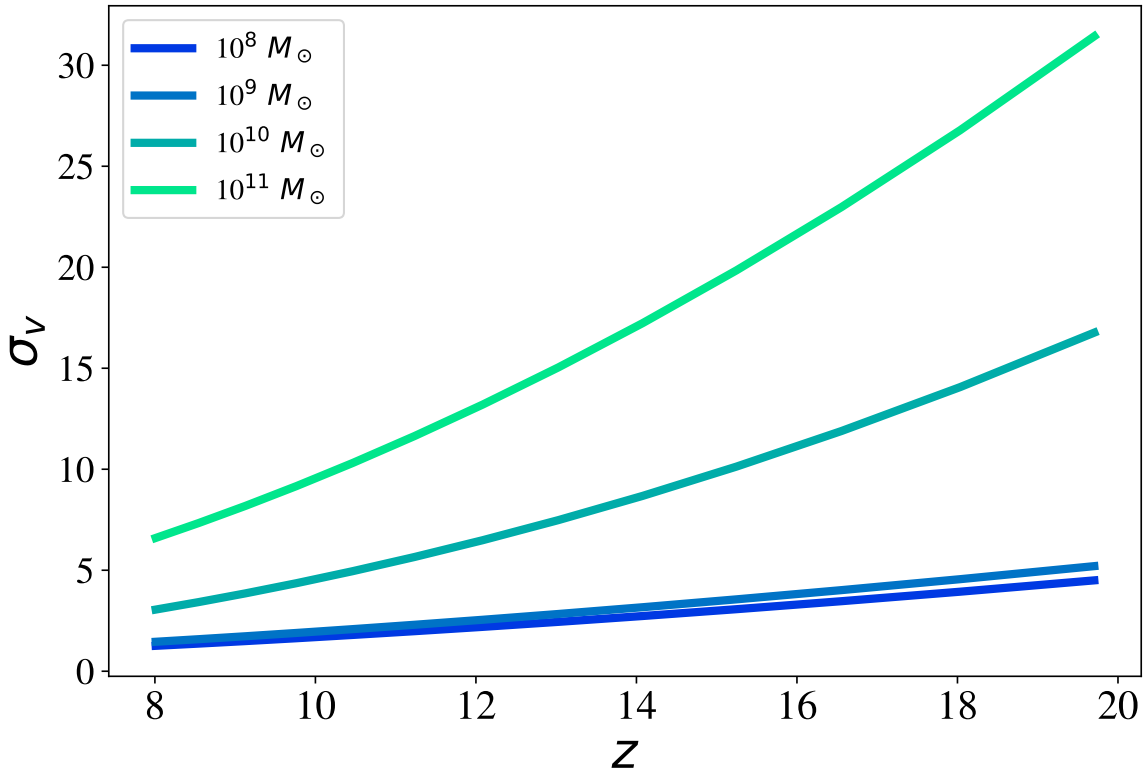

Figure 5: Cosmic variance σ_v as a function of redshift for a single $2.1' \times 2.1'$ NIRCam pointing. Note the fact that σ_v drastically increases as both a function of redshift and mass, meaning that discovering a high mass galaxy at high redshifts becomes increasingly uncommon in surveys with small areas.

4 The Halo Mass Function

The Halo Mass Function (HMF) describes the number density of dark matter halos in a given mass range $[M, M + dM]$, within a given finite comoving volume V_c. Understanding this distribution is invaluable to the search for ultra-high redshift galaxies, as it allows us to quantify the expected number and mass distribution of mock surveys. Comparing it against observational findings can also allow us to test our current cosmological models given that matter density controls the rate at which large scale structures grow, making it very sensitive to cosmology (Behroozi & Silk, 2018; Boylan-Kolchin, 2023a; Ezquiaga et al., 2023).

The HMF was determined by measuring the number density of halos within a variety of N-body simulations (Press & Schechter, 1974; Jenkins et al., 2001). The number of halos with mass less than M, which is defined as $n(M)$, was taken in each simulation, and is often expressed in differential form dn/dM,

$$\frac{dn}{dM} = f(\sigma)\frac{\overline{\rho}_m}{M}\frac{d\ln\sigma^{-1}}{dM} , \tag{38}$$

where over the years, $f(\sigma)$ has been parameterized in a plethora of ways (see Table 1 of Murray et al. (2013) for a comprehensive list), however Bond et al. (1991) found that it can be expressed in the relatively simple form by assuming that the halos form by spherical collapse:

$$f(\sigma) = \sqrt{\frac{2}{\pi}}\frac{\delta_c}{\sigma}\exp\left(-\frac{\delta_c^2}{2\sigma^2}\right) , \tag{39}$$

where δ_c is the critical over-density for a halo being formed by spherical collapse (found to be $\delta_c \simeq 1.686$), and

$$\sigma = \int P(k)\hat{W}(kR)k^2 dk , \tag{40}$$

where $P(k)$ is the power spectrum with respect to the wavenumber k, and $\hat{W}$ is the Fourier transform of a top hat function of radius R. In this case, σ is the rms variance of the mass M contained within a sphere of radius R, and is not to be

confused with cosmic variance σ_v. The values A, b, and c are fit for a given overdensity parameter Δ. Although a Press-Schecter function was originally used to model the HMF (Haslam et al., 1964), Lukić et al. (2007) compared the different forms of $f(\sigma)$, and concluded that the Press-Schecter function underestimates the number of massive dark matter halos at high redshifts, and conversely underestimates the number of low mass halos at low redshifts. This resulted in the adoption of the Sheth et al. (2001) definition of $f(\sigma)$, which assumes an ellipsoidal halo collapse, and accounts for the differences between the Press-Schecter function and the findings of the N-body surveys, defined as

$$f(\sigma) = A\sqrt{\frac{2a}{\pi}}\left[1 + \left(\frac{\sigma^2}{a\delta_c^2}\right)^p\right]\frac{\delta_c}{\sigma}\exp\left(-\frac{a\delta_c^2}{2\sigma^2}\right), \tag{41}$$

where $A = 0.3222, a = 0.707, p = 0.3$ (Sheth et al., 2001).

5 Models and Methodology

This work employs 3 key models in order to achieve its end result: 1) the extrapolated luminosity function into the $z > 8$ regime, 2) the lens models of massive galaxy clusters modelled using *HST/JWST* data, and 3) lens models of massive mock elliptical galaxies using `LENSTOOL`. This section will explore these models and the methods in which they were used to build our mock survey code.

A flat ΛCDM cosmology was assumed, with $h = 0.677$ and $\Omega_m = 0.3$.

5.1 The Luminosity Function

The luminosity function (LF), which is the number density of galaxies $\phi(M)$ as a function of their apparent UV luminosity (m_{UV}) was extrapolated from high-redshift *HST* surveys to estimate the $z > 8$ regime. The result of Bouwens et al. (2015) found the resulting luminosity function after fitting observed luminosity functions for $z \sim 4 - 10$ with a Schecter function:

$$\begin{aligned} \phi(M) &= \phi^* \frac{ln(10)}{2.5} 10^{-0.4(M-M^*)(\alpha+1)} e^{-10^{-0.4(M-M^*)}} \\ M^*_{UV} &= (-20.95 \pm 0.10) + (0.01 \pm 0.06)(z-6) \\ \alpha &= (-1.87 \pm 0.05) + (-0.10 \pm 0.03)(z-6) \\ \phi^* &= (0.47^{+0.11}_{-0.10}) 10^{(-0.27 \pm 0.5)(z-6)} 10^{-3} Mpc^{-3} \ . \end{aligned} \tag{42}$$

These fits were used to extrapolate the LF to $z > 10$, and the substantial uncertainties at $z >> 6$ were reported in Fig. 3 of Steinhardt et al. (2021). Next, the UV LF was converted to a stellar-mass LF in accordance with Song et al. (2016), which fit a linear relation between M_{UV} and log($M_*/M_\odot$). Following Song et al. (2016), the best fit slope at $z = 8$ was used for $z > 8$, along with the intercepts of the linear fit of the data between $4 < z < 8$, resulting in a universal mass-to-light ratio for a fixed redshift.

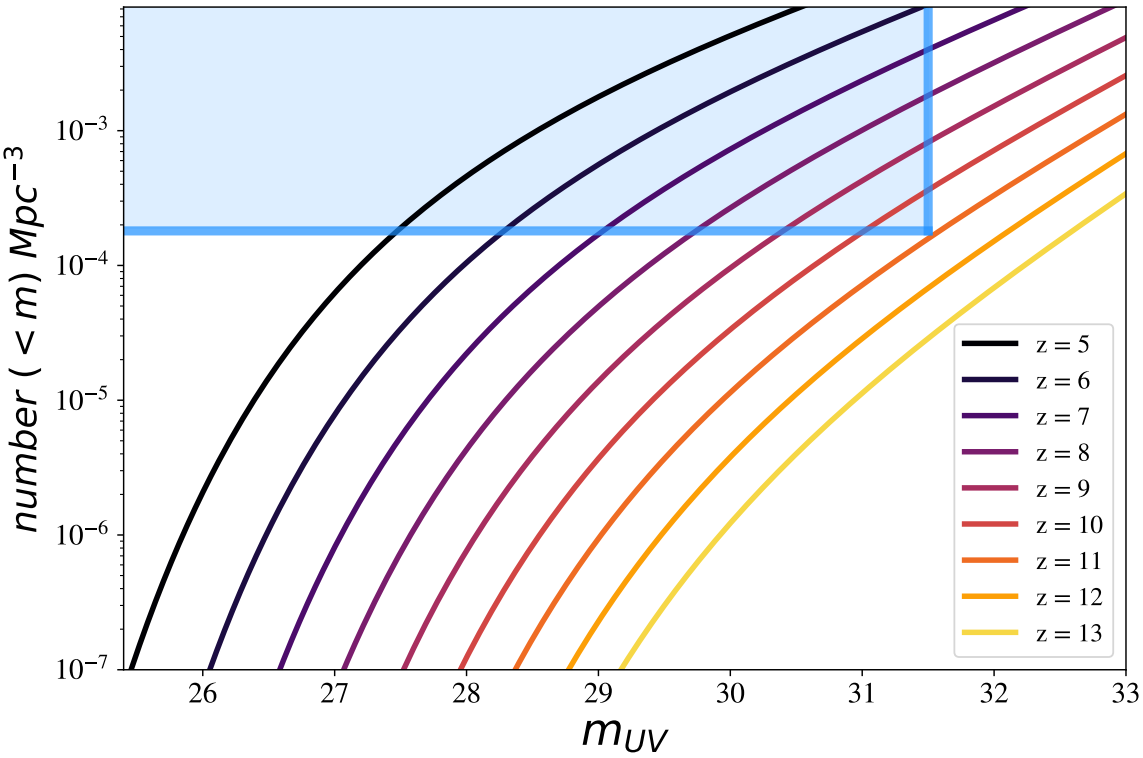

Figure 6: Luminosity functions centered at a variety of redshift bins, computed for a single JWST NIRcam pointing (2.1'x2.1'). The blue shaded region represents the visible region of the LF as seen within a single JWST observation at a depth of $m_{UV} = 31.5$. For a survey of this size and limiting magnitude, the blue box shows that the highest redshift object that one could detect lies at $z \sim 11$.

5.2 Galaxy Cluster Models

The galaxy cluster models were generated from the publicly available products from the CLASH/MUSES catalogues (Zitrin et al., 2015; Richard et al., 2021), which utilized combinations of strong and weak gravitational lens modelling codes such as `LENSTOOL`, as well as the LTM method outlined in Zitrin et al. (2009, 2015); Broadhurst et al. (2005); Zitrin et al. (2015). Clusters were selected from these surveys due to them containing the most massive known galaxy clusters, and their plethora of multi-wavelength observations, which has enabled accurate modelling the lenses. The light-traces-mass assumption (LTM) simply implies that the mass

distribution of both the cluster and member galaxies is reasonably traced by the cluster's light distribution (Broadhurst et al., 2005; Zitrin et al., 2015), and is used as a starting point for fitting the locations and distributions of dark matter in the cluster. The models for El Gordo were calculated using new *JWST* NIRCam imaging of the cluster, in conjunction with a free form lensing construction code WSLAP+ (Diego et al., 2005, 2007, 2015, 2022; Sendra et al., 2013). This model, which does not rely on assumptions about the distribution of dark matter, was found to be consistent with previous parametric models (Diego et al., 2023).

The provided maps were pre-scaled to a fiducial redshift of $D_{LS}/D_s = 1$. Therefore, in order to re-calculate the magnification factor for a source at $z = 20$, we must re-scale both the convergence κ, as well as the shear parameter γ using our new value of D_s for a source at $z = 20$.

This results in the new equation for the magnification factor μ:

$$\mu = \left[(1 - (D_{LS}/D_s)\kappa)^2 - ((D_{LS}/D_s)\gamma)^2\right]^{-1}, \tag{43}$$

which allowed us to use the κ and γ maps from Zitrin et al. (2015), Richard et al. (2021), and Diego et al. (2023) to compute the magnification maps for our target source at $z = 20$, as seen in Fig. 8.

5.3 Elliptical Galaxy Models

The models for individual elliptical galaxy lenses were created using the aforementioned `LENSTOOL`, with which various combinations of masses M_{200}, concentrations c_{200}, and galaxy redshift z_L were used to find the ideal combination suited for finding ultra-high redshift galaxies.

As per Diemer & Kravtsov (2015), large elliptical galaxies maintain a concentration factor of approximately $c_{200} \sim 5 - 6$. Therefore, in order to pursue an ideal candidate, the concentration factor was fixed at $c_{200} = 6$, the ellipticity to $e = 0.25$, and we tested two different masses, $M_{200} = 10^{12} M_\odot, 10^{13} M_\odot$, as well as 4 different galaxy redshifts $z_L = 0.4, 0.6, 0.8.1$. All models were tested, however the only

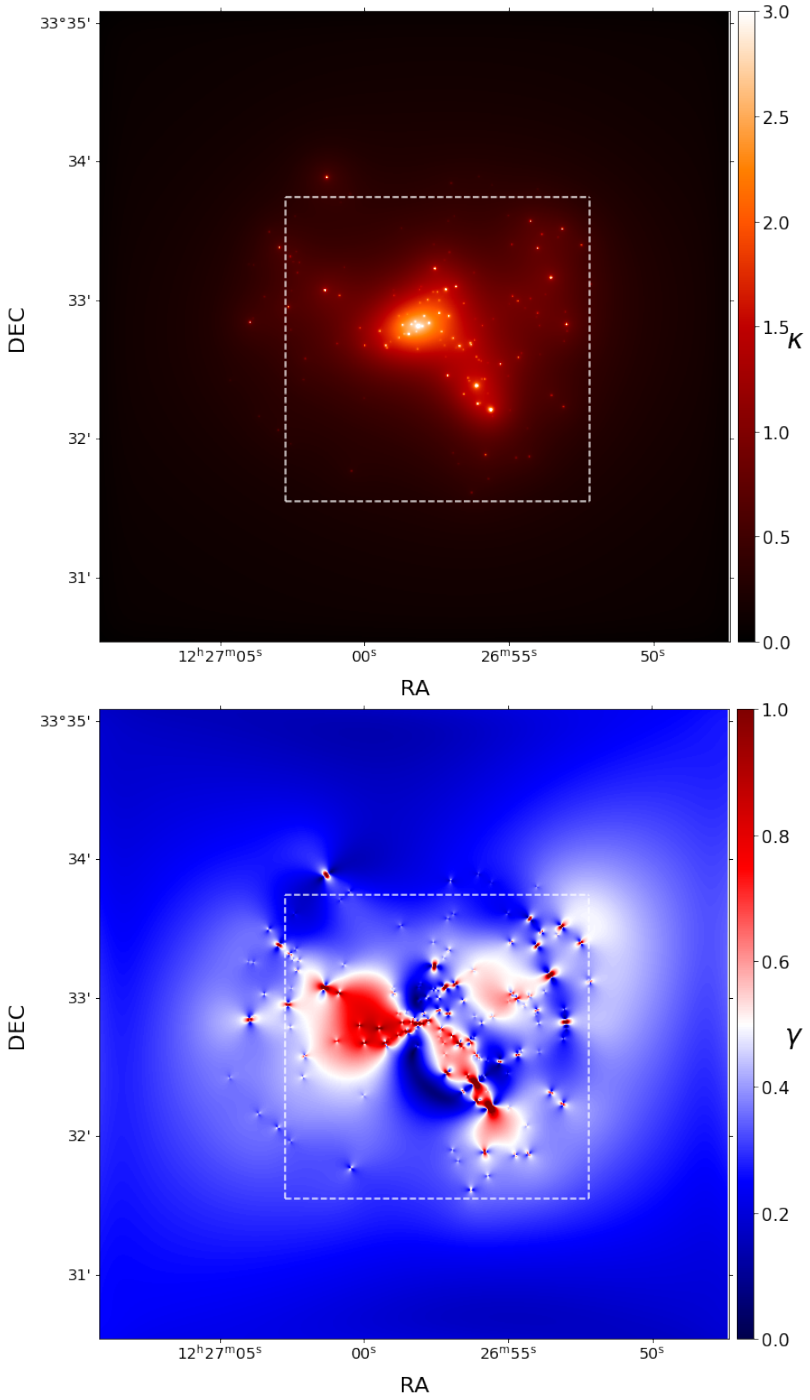

Figure 7: Example of a convergence map (κ) and a shear parameter map (γ) for the galaxy cluster CLJ1226.9+3332, scaled for a fiducial redshift where $D_{LS}/D_s = 1$. The white dashed lines correspond to the field of view of a single NIRCam pointing (2.1'x2.1').

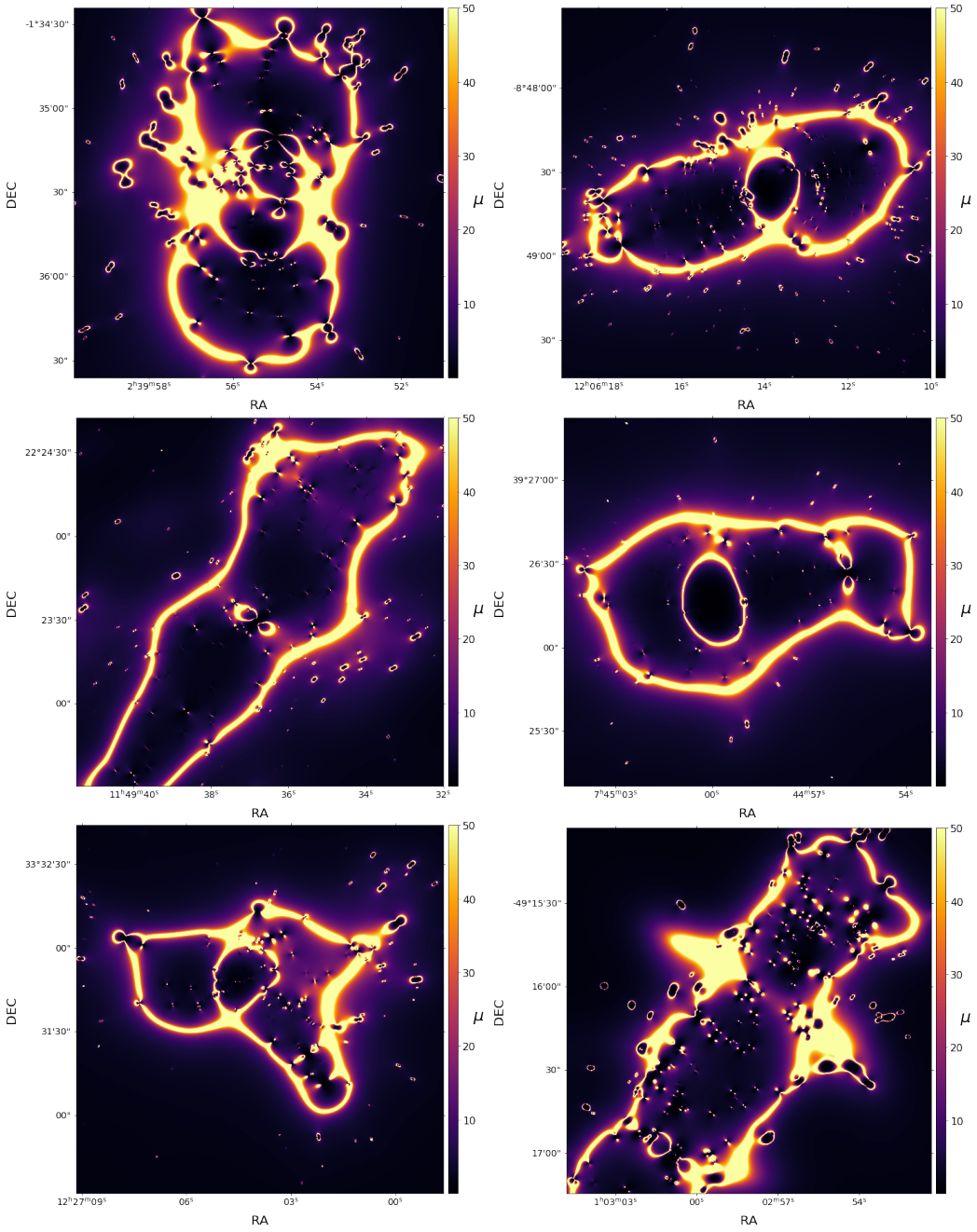

Figure 8: Magnification maps (μ) within a single NIRCam pointing (2.1'x2.1') of Abell 370 (top left), MACS J1206.2−0847 (top right), MACS J1149.5+2223 (middle left), MACS J0744.9+3927 (middle right), CL J1226.9+3332 (bottom left), and El Gordo (bottom right). Note that these 6 galaxy clusters occupy nearly the entirety of the pointing with high magnification factors.

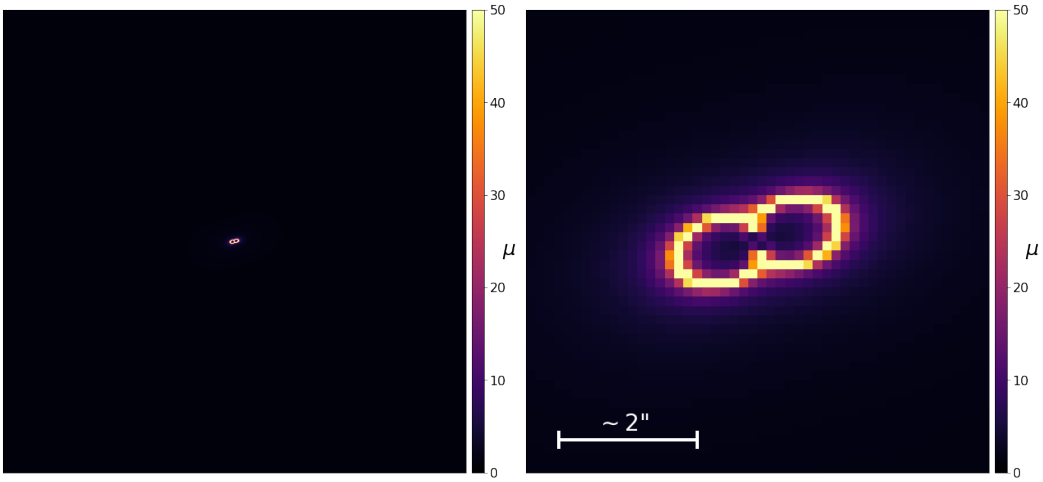

Figure 9: Magnification map (μ) of an elliptical galaxy of mass $M = 10^{13} M_{\odot}$ as seen in a single NIRCam pointing (2.1'x2.1'), scaled for a source at $z = 20$ (left), as well as a zoomed in version (right). Notice the minuscule amount of the field of view that the resulting magnification map occupies as opposed to those generated by the galaxy clusters in Fig. 8.

model with significant benefits to our study was the ideal case of a galaxy with $c_{200} = 6, M_{200} = 10^{13} M_{\odot}, z_L = 1$. The magnification map μ for this example can be seen in Fig. 9.

5.4 Implementation of Magnification Maps

The magnification maps generated by either the galaxy cluster or elliptical galaxy lens models can be implemented into our mock survey code in order to model the benefits that magnification factors have in detecting high-redshift sources. Although Steinhardt et al. (2021) took the mean magnification factor of a lensed field into account in their mock survey trials, they did not take into account the randomness that is inherently associated with searching for high-redshift targets behind foreground lenses. As seen in Fig. 8, the magnification factors vary drastically within the field of view, therefore the mean or median magnification factor is not an adequate representation of the effects of the magnification factors within the field.

In its original form, the mock survey code (Steinhardt et al., 2021) computed the mean number of objects one would expect to see within a given survey volume (before taking cosmic variance into account) by integrating the luminosity function for every mass bin over the range of apparent magnitudes that would be visible by the given instrument. In this case, the maximum limiting magnitude of JWST $m_{JWST} = 31.5$ was used. An important note is that the mass bins were chosen to be the same as those selected by Moster et al. (2011) in order to be able to calculate the cosmic variance associated with those masses ($M = [7.0 - 11.0]$ log $(M_{\odot})$, $\Delta M = 0.5$ log $(M_{\odot})$). This work also made use of the `cosmic-variance`[1] python package, which is a python adaptation of the original IDL code released with Moster et al. (2011).

In order to attempt to model the random locations of background sources, during the step where the luminosity function is integrated up until a fixed limiting magnitude, a random pixel from the magnification map is drawn and converted into the new limiting magnitude

$$m_{lim,new} = m_{lim,old} - (-2.5 \log(\mu)) \,, \tag{44}$$

where $m_{lim,old}$ is the limiting magnitude of the survey and μ is the random magnification factor drawn from the magnification map of the foreground cluster. Now, every mass bin has an independent limiting magnitude over which the luminosity function will be integrated. This process will repeat for every redshift bin in order to introduce as many independent source locations within the pointing. Fig. 10 shows an example instance of the 126 random points (due to the fact that the survey code uses 14 redshift bins and 9 mass bins) within the μ maps that are selected by the mock survey code, where the green stars represent the randomly selected magnification factors. One can see that the random magnifications drawn from such a strong lensing field will vary drastically, and will most likely not resemble the mean or median magnification factor given the steepness of the magnification factor around the critical lines.

[1] https://pypi.org/project/cosmic-variance/

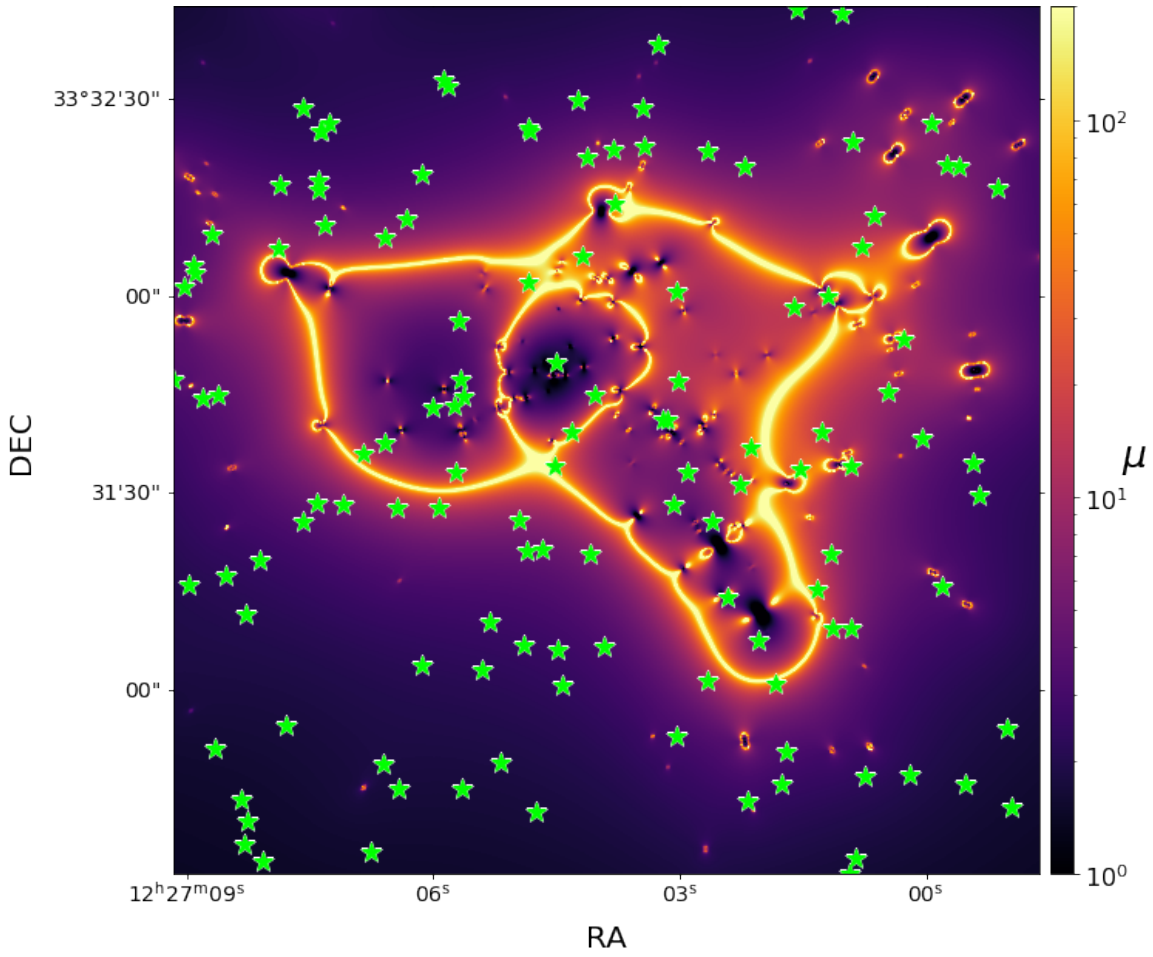

Figure 10: Magnification map (μ) of CL J1226.9+3332, where the green stars represent an example of the 126 random magnification factors selected within the mock survey code. Note the drastically different magnification factors from one draw to another.

6 Comparative method for selecting the ideal survey strategy

Three survey types were compared in order to determine their relative efficiencies in finding high-redshift galaxies: using foreground massive galaxy clusters, massive foreground elliptical galaxies, and a larger "snapshot" style of survey with a lower integration time but significantly larger search area, such as the JADES Medium Robertson et al. (2022), which has proven to be successful in finding $z \approx 12$ galaxy candidates using a combination of photometry and spectroscopy.

Testing was conducted using a modified version of the code created by Steinhardt et al. (2021), which was updated to accept magnification maps from various foreground sources in order to simulate the magnification effects from strong gravitational lenses on the number of galaxies found, and the maximum distance redshift (z_{max}) we can expect to see galaxies in each field. The four main results which were used to compare the efficacy of each survey design were the distribution of magnification factors above a given threshold within the field, the median magnification factor of each cluster within the single pointing, the mean and median highest redshift galaxy found in each iteration (z_{max}), and the number of galaxies found within each redshift bin.

When comparing the lensed cases, it is obvious that the massive galaxy clusters would outperform the massive elliptical galaxies in terms of strength of lensing and magnification factors. However, the major limitation in the cluster lensing case is the number of high quality foreground clusters that would be suitable for this type of survey. There are significantly more high mass, high concentration elliptical galaxies in the target redshift region for an ideal foreground cluster ($z \approx 1$) than there are massive clusters. Given the importance of the number of independent lines of sight to combat the effects of cosmic variance, this will significantly benefit the cases of both the foreground elliptical galaxies, as well as the blank field snapshot programs.

6.1 Blank Field Snapshots

As per the findings of Steinhardt et al. (2021), proposed JWST surveys of blank fields, such as JADES or CEERS, are likely to find galaxies up to a median redshift of $z \sim 12 - 14$ depending on the survey strategy.

Early releases from the JADES survey have already yielded a record breaking galaxy JADES-GS-z13-0 at $z_{spec} = 13.2$ (Robertson et al., 2022), which was originally discovered photometrically using NIRCam, but who's Lyman break was confirmed spectroscopically using NIRSpec shortly afterwards.

The CEERS survey (Finkelstein et al., 2023) is similarly dedicated to finding large samples of galaxies in the $8 \leq z \leq 13$ range, covering a field of view of ~ 100 arcmin^2 with NIRCam, to maximum depths of ~ 29.15 for a 5σ point source[2]. CEERS has even found a $z_{phot} \sim 16.4$ candidate galaxy (Finkelstein et al., 2022; Donnan et al., 2022; Naidu et al., 2022; Harikane et al., 2023; Finkelstein et al., 2023; Bouwens et al., 2023), which unfortunately was spectroscopically confirmed using NIRSpec to be at $z \sim 4.9$ (Haro et al., 2023).

These early *JWST* surveys have proven to be effective methods of finding high redshift galaxies, in part because they employ wide search areas (46 -190 arcmin^2), with limiting magnitudes of 30.7-29.8 mag. respectively. The benefits of such a survey strategy is that the effects of cosmic variance are significantly weaker with large survey volumes. However, both of these surveys required large time allocations in order to achieve high limiting magnitudes over large survey areas. Because cosmic variance favors independent lines of sight as opposed to large spatially coherent search areas, the search for high-z galaxies would have greatly benefited from independent lines of sight with similar time allocations.

[2] https://ceers.github.io/obs.html

7 Selecting the optimal foreground clusters for finding ultra-high redshift galaxies

Since the background galaxies being magnified lie at a greater distance, the optimal foreground clusters for lensing the $z \sim 15 - 20$ galaxies we hope to discover with *JWST* will be different than those optimal for finding $z \lesssim 10$ galaxies with *Hubble*.

In this work, the six optimal foreground clusters were selected based on three simple metrics: the fraction of pixels within a single 2.1'$\times$2.1' pointing that fall above a given magnification factor (Fig. 11), the probability distribution of the highest redshift galaxy discovered, and the median highest redshift found in simulated lensed pointings. Thus, the clusters proposed here are those with the greatest probability of discovering the highest-redshift targets with the fewest pixels 'wasted' due to low magnification.

Not surprisingly, the three most efficient foreground clusters are Abell 370, El Gordo (also known as ACT-CL J0102-4915 or SPT-CL J0102-4915), and MACS J1149.5+2223, which already have upwards of 80 hours of *JWST* time dedicated to imaging in existing programs. These clusters are both incredibly massive (both with $M_{vir} > 10^{15} M_{\odot}$), and concentrated ($c_{200} \approx 3.3, 5$) for Abell 370 and MACS J1149.5+2223 respectively. Being at lower redshifts, they have had more time for their structures to relax and create more efficient lenses. We also used the next three optimal foreground clusters: CLJ 1226.9+3332 ($z \sim 0.890$), MACS J0744.9+3927 ($z \sim 0.686$), and MACS J1206.2−0847 ($z = 0.4385$).

The candidate clusters were selected from the CLASH (Postman et al., 2012) program and have VLT/MUSE observations (Richard et al., 2021). Thus, there is prior confirmation that these are indeed strong lensing clusters, with the added benefit of having a wealth of spectroscopic and photometric data already available at shorter wavelengths. The mass and magnification maps for each cluster candidate were generated from the publicly available CLASH and MUSE products, re-scaled for a source at $z = 20$, then cut to the NIRCam pointing size (2.1'x2.1').

The six best candidates have median magnification factors of $\mu \sim 6.0$ (Abell 370), $\mu \sim 5.2$ (MACS J1149.5+2223), $\mu \sim 4.6$ (MACS J0744.9+3927), $\mu \sim 4.6$ (MACS J1206.2−0847), $\mu \sim 4.6$ (El Gordo), and $\mu \sim 3.5$ (CL J1226.9+3332) for sources at $z = 20$.

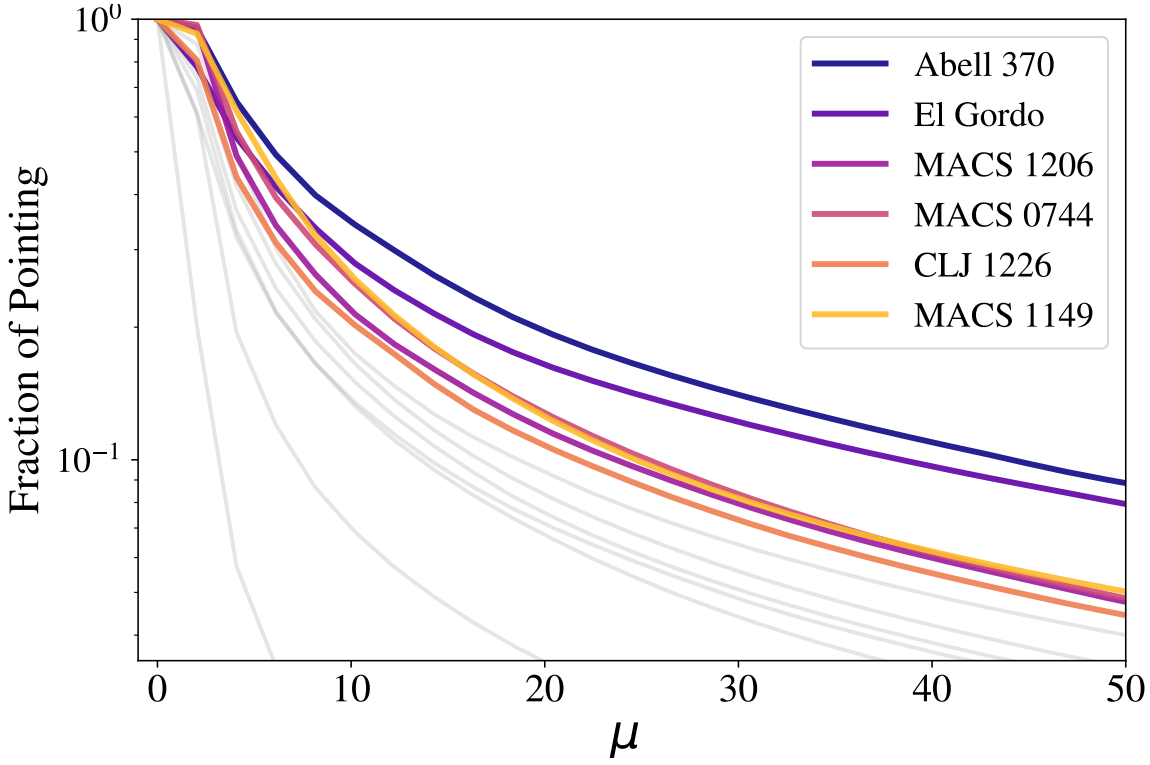

Figure 11: Fraction of NIRCam pointing covered by magnification factors greater than μ. The gray lines correspond to the next-best known clusters: Abell 2744, RXJ 1347-1145, MACS J0257.1-2325, MACS J2214.9-1359, MACS J0416.1-2403, Abell 209, and Abell 2261. The 6 clusters that were selected occupy the highest fraction of pixels within the pointing with high magnification factors.

More generally, these 6 clusters will magnify the highest fraction of their pointing for any large magnification factor μ (Fig. 11). These are therefore also the most efficient foreground clusters for selecting targets requiring higher magnification, and thus the best new discovery tool for fainter high-redshift sources as well.

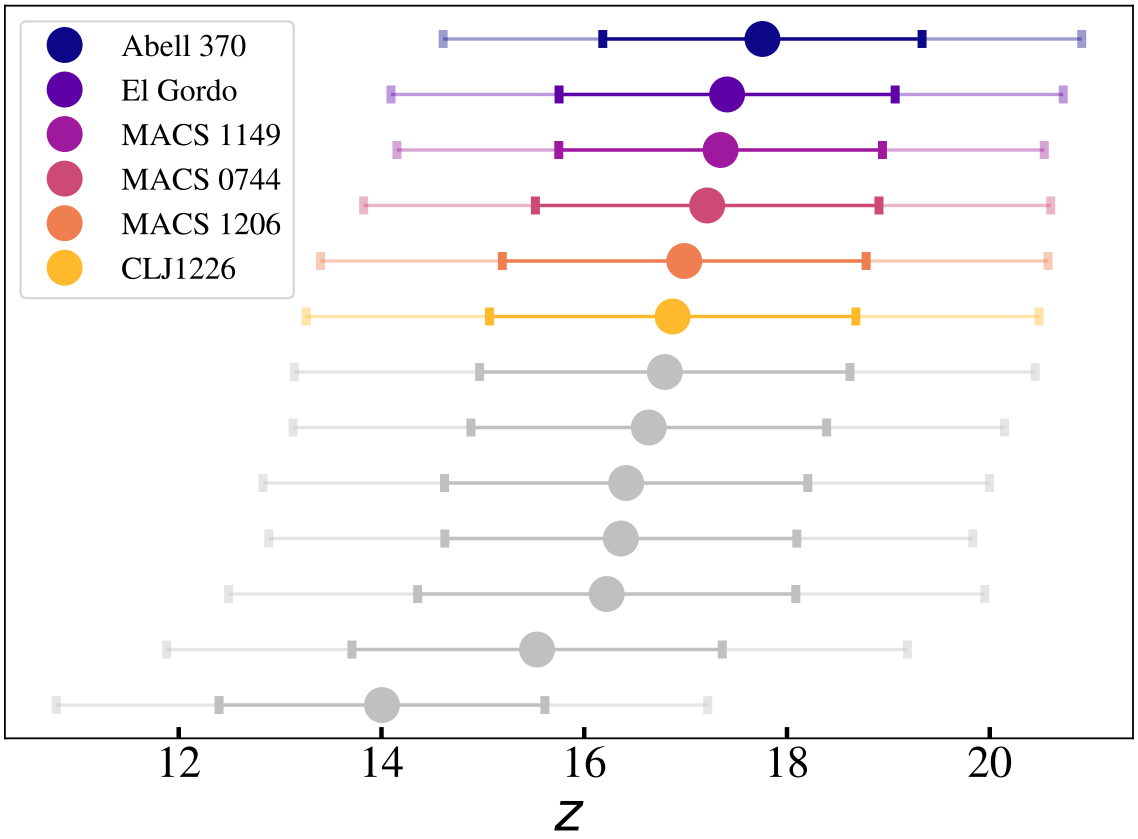

Figure 12: Mean highest redshift galaxy found over 500 iterations for each cluster, where the solid errorbar represents equivalent percentages to 1σ of the distribution, and the lighter error-bar represents 2σ. Shown for comparison (gray) are the next-best CLASH/MUSES clusters: RXJ 1347-1145, Abell 2744, MACS J2214.9-1359, MACS J0257.1-2325, MACS J0416.1-2403, Abell 2261, and Abell 209 respectively. The pointings containing the 6 optimal galaxy clusters yielded on average the detection of the highest redshift galaxy when compared against the next best clusters.

An additional effect of the high cosmic variance is that a small fraction of pointings will contain a strong overabundance of massive, ultra-high redshift galaxies, while most of the remainder will contain none. Although the disadvantage is that this requires many independent sightlines for an initial discovery, it also implies

that a single, massive ultra-high redshift galaxy is likely to lie in a rich field with many lower-mass companions at similar redshift. Thus, a robust discovery of a single high-mass, ultra-high redshift galaxy can be used as a signpost pointing the way to an ideal target for deeper followup observations.

8 The Ideal Survey Strategy

The results of our study conclude that the clear choice for a survey optimized to find ultra-high redshift galaxies is using multiple lines of sight containing massive foreground galaxy cluster lenses.

Foreground Cluster	Median z_{max}	Mean z_{max}	$P(z > 15)$	$P(z > 17)$
Abell 370	18.03	17.76	98.2%	60.2%
MACS 1149	16.56	17.34	96.6%	49.6%
MACS 1206	16.56	16.99	91.2%	44.4%
MACS 0744	16.56	17.21	93.8%	46.6%
El Gordo	16.56	17.21	96.0%	51.4%
CLJ 1226	16.56	16.87	89.4%	39.0%

Table 1: Highest redshift galaxy found in the median and mean simulated survey for each 2.1'x2.1' line of sight along each foreground cluster, as well as the percentage of finding a galaxy above $z \sim 15$ and $z \sim 17$ over 500 trials.

Survey	Median z_{max}	Mean z_{max}	$P(z > 14)$
JADES (M)	12.09	12.27	1.8%
JADES (D)	13.03	12.95	17.2%
CEERS	10.47	10.48	0%

Table 2: Highest redshift galaxy found in the median and mean simulated blank field surveys, as well as the percentage of finding a galaxy above $z \sim 14$ over 500 trials. Note that the mean and median z_{max}, as well as the probability of finding an ultra-high redshift galaxy are significantly lower than those of the optimal cluster fields in Tab. 1.

As summarized in Tables 1 and 2, lines of sight containing galaxy clusters optimized for magnifying high-redshift galaxies significantly outperform *JWST* blank field surveys such as JADES or CEERS, which are specifically designed to find high-redshift galaxies.

The pointings containing the ideal galaxy clusters not only provide the highest probability of finding an ultra-high redshift galaxy, but the strong magnification factors present along these lines of sight could allow for the highest redshift galaxy

that *JWST* could possibly detect. This is in spite of the strong effects of cosmic variance in the $15 \leq z \leq 20$ regime, which the large area blank field surveys aim to combat.

Another distinct benefit to using single, deep JWST pointings as opposed to combining many of them in order to cover large patches of the sky is that one could observe multiple clusters in the same time that it takes to observe one large patch of the sky.

For example, if it takes 10 hours of NIRCam photometry to reach its maximum limiting magnitude in a single pointing, a blank field survey comprised of 10 NIRCam pointings such as CEERS would require 100 hours of photometry (not including overheads) in order to detect a galaxy up to $z \sim 14$. Even in this case, the pointings are side by side and not independent, therefore you would not be negating the effects of cosmic variance in the most optimal manner for the high-redshift regime. However, if you were to use the same 100 hours of photometry time looking at galaxy clusters, you would not only be able to observe the 6 clusters presented in this work at maximum depth, but also the 4 next best clusters (which can be seen in Fig. 12) in the same amount of time. Not only are you statistically more likely to find a $z \geq 15$ galaxy in this manner (as seen in Table 1), but you would benefit from completely independent lines of sight between the different clusters, thus providing the added benefits of optimally combating cosmic variance.

9 Future Work

This section explores future work that such a survey would enable.

9.1 Elliptical Galaxies with Excess Near Infrared Emission as candidate foreground lenses

Similar tests to those done with the galaxy clusters in section 5.2 were conducted for simulated elliptical galaxies, using the parameters specified in section 5.3. Although it was found that the lensing efficiency was drastically lesser than that of a galaxy cluster, it was found that an elliptical galaxy of mass $M = 10^{13} M_{\odot}$ at a redshift of $z = 1$ gives a 1% chance of finding a $z > 15$ source in the background. However, the benefit to using elliptical galaxies as foreground lenses is that there is a significantly larger number of suitable lensing galaxies than clusters, meaning that the large number of independent lines of sight could help mitigate the effects of cosmic variance at high redshifts. A potential survey strategy to optimize the search for high-redshift sources using elliptical galaxies as foreground lenses would be to use massive elliptical galaxies containing evidence of excess near-infrared emission, which could potentially be caused by a high-redshift background source being magnified by the foreground galaxy.

An important precursor to using such a galaxy as a foreground lens would to to first use photometric observations of the galaxy to identify strong lensing features surrounding the galaxy. This would help verify that the excess NIR emission could be caused by a background source and not just local effects. Assuming that the emission is indeed caused by such background source, we would expect to the background source to lie very close to the strong magnification factor regime of the foreground lens. This would allow us to observe a potentially ultra-high redshift source, along with using the shears caused by the lensing effects to constrain the dark matter halo of the foreground galaxy. Due to the small fraction of a NIRCam pointing being covered by the strong lensing regime of a single massive elliptical galaxy (as seen in Fig. 9), we would need a substantial number of massive foreground elliptical galaxies in order to compete with the lensing benefits of a single massive galaxy cluster. Although the probability of the NIR excess being caused by a background high-redshift galaxy is small, we would only need ~ 270 candidates to match the chances of finding a source at a redshift $z > 15$ to that of the

clusters analyzed in this work. Although this number is high, the benefit is that due to cosmic variance, there is still a chance that none of the aforementioned clusters contain ultra-high redshift background sources. Because of the limited amount of high-quality lensing clusters, the additional uncorrelated lines of sight provided by the elliptical galaxies could benefit in the search for these high-redshift galaxies.

However, our study also showed that the probability of finding galaxies of redshift $z > 16$ in using elliptical galaxies is nearly non-existent due to the small amount of the NIRCam pointing that the strong lensing regime covers (Fig. 9). Therefore, although they are suitable for finding high redshift galaxies, they are statistically unlikely to find as high of a redshift galaxy as galaxy clusters.

9.2 Massive Galaxies as a Probe of ΛCDM

A series of recent studies have found hints of tension between the most massive high-redshift galaxies and the standard ΛCDM cosmological paradigm. The first stage in galaxy formation is the assembly of a compact halo, and the ΛCDM halo mass function is well constrained via numerical calculation (Sheth et al., 2001; Vogelsberger et al., 2014). Subsequent processes turn the assembled baryons into stars and other structures that become recognizable as a galaxy.

However, the most massive sources at $z > 4$ from *Hubble* are so massive, so early, that there should not yet have been time for their halos to finish assembling, let alone to further turn their baryons into stars (Steinhardt et al., 2016). This "impossibly early" galaxy problem was sharpened by the discovery of high-redshift, massive quiescent galaxies (Glazebrook et al., 2017). One proposed resolution was an increased stellar baryon fraction for the first galaxies (Finkelstein et al., 2015; Behroozi & Silk, 2018). However, the tension increases towards high redshift, and initial *JWST* studies reported $z \sim 10$ galaxies so massive that even if all of their baryons had already ended up in stars, they would still be too massive to reconcile with the ΛCDM halo mass function (Labbé et al., 2023; Boylan-Kolchin, 2023b). Although these redshifts and masses are not yet robustly proven (Steinhardt et al., 2022; Zavala et al., 2023), it is clear that the most massive, earliest

galaxies will provide a stringent test of the ΛCDM halo mass function and thus of ΛCDM. For this reason, a survey of a medium depth would be optimal for discovering this high-mass tail.

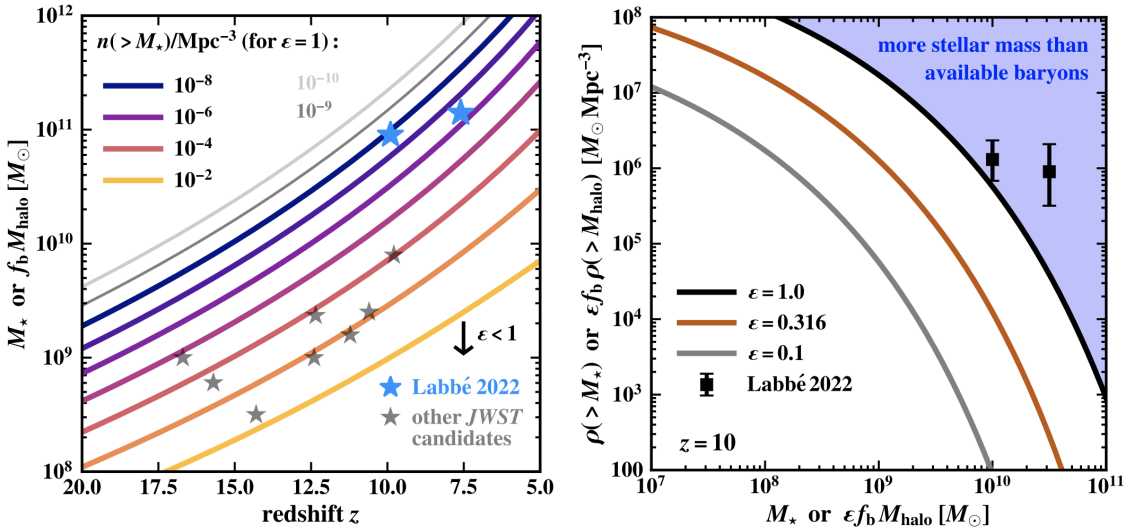

Figure 13: (Reproduced from Boylan-Kolchin (2023a)). The most massive, highest-redshift galaxies from the first JWST studies appear to be in tension with the predictions of ΛCDM. Although follow-up studies have produced different stellar masses and redshift for many of these individual targets, the robust discovery of an impossibly massive high-redshift galaxy would require changing the cosmological model. The suggested clusters are optimized for finding the high-mass tail of the stellar mass function at $z > 15$.

9.3 The value of crossing the $z \sim 15$ threshold

When pursuing the search for the most distant galaxy, it is important to consider the value in finding a $z \sim 17 - 18$ galaxy, such as is statistically likely in a cluster-lensed field, as opposed to a $z \sim 14$ that could be found in a blank field. The range of redshifts between $15 \leq z \leq 20$ is incredibly important because our current cosmological models have placed the formation of the first galaxies in the universe

to be within this regime (Visbal et al., 2012; Yung et al., 2023; Lacey et al., 2011; Bromm & Yoshida, 2011; Springel et al., 2005). Thus, being able to find any galaxy in this redshift regime would be invaluable in constraining these models of early universe galaxy formation, as well as providing insight into the formation of the first generation of stars. Observing galaxies in this redshift regime could also lead to observational confirmation of Pop III stars, which are a hypothetical population of high-mass, low metallicity stars that are theorized to have formed around $20 \leq z \leq 30$ (Haiman et al., 1997; Barkana & Loeb, 2001; Bromm et al., 2002; Visbal et al., 2018). Observing these Pop III stars would be invaluable to understand the enrichment of the ISM in the early Universe, which led to the creation of the significantly more abundant Pop II stars which we can observe today. However, verifying the end of the cosmic dark ages would need to be confirmed with multiple sight-lines in order to get a robust limit.

9.4 Mapping the Baryonic and Dark Matter Distributions

High quality photometry of the proposed clusters will be invaluable in constraining the distribution of baryonic and dark matter in clusters, continuing the prior success of the Hubble Frontier Fields (Lotz et al., 2017) and followup programs. The three high redshift clusters CL J1226.9+3332 $(z = 0.890)$, El Gordo $(z = 0.87)$, and MACS J0744.9+3927 $(z = 0.686)$ would be particularly important targets, since they probe an earlier stage of the hierarchical merging process that leads to the formation of massive clusters than probed by existing studies. Although the massive clusters that we see in the local universe have been built through major mergers, they have subsequently relaxed. Being able to obtain high resolution photometry of clusters at an earlier stage will allow us to probe the dynamics of these major mergers, as well as place the best constraints on dark matter distributions within the clusters and possible interactions between dark matter and baryons.

Scaling relations between baryonic properties and dark matter predicted in cosmological simulations evolve with redshift (Zavala & Frenk, 2019). Comparing these predictions with observations, in particular at high redshifts, is essential for

understanding the underlying mechanisms regulating the distribution of baryons and dark matter. These scaling relations are also used as cluster mass proxies in cosmological constraints from the cluster mass function (Lovisari & Maughan, 2022; Allen et al., 2011). Independent direct tests of these relations at high redshift are necessary in order to control the accuracy of cosmological measurements based on the cluster mass function (Bulbul et al., 2019; Vikhlinin et al., 2009).

The unprecedented depth of *JWST* images of the suggested high-redshift clusters will enable us to quantify the difference between baryonic and dark matter distributions in galaxy clusters. Analysis of low-redshift clusters shows that their lensing potential cannot be reproduced without assuming a smooth large-scale dark matter component independent of the baryonic distribution (e.g., Limousin et al. (2022); Ghosh et al. (2021); Jauzac et al. (2018)). These observations would enable us to study this at much higher redshift, further constraining models for dark matter-baryon interactions.

Cluster strong-lensing cosmography is an additional promising probe of cosmological parameters, including the dark energy equation of state. Observations of a single galaxy cluster constrain only a combination of selected parameters. An effective way to break this degeneracy is to observe several clusters spanning a wide range of redshifts. The current constraints are based on 5 strong lensing clusters at relatively low redshift (Caminha et al., 2022). We expect that observations of numerous galaxies lensed by the highest-redshift clusters suggested in this work such as MACS 0744, CLJ 1226, and El Gordo will provide significant additional constraining power for cluster strong-lensing cosmography.

Acknowledgements

First and foremost, I would like to thank my supervisor Charles Steinhardt, not only for helping me throughout the research process, but for fueling my curiosity, and encouraging me to pursue new and exciting challenges like leading an observing proposal.

Additionally, there are many people that I would like to thank for their contributions to both my thesis, and the resulting observing proposal: Vadim Rusakov, Albert Sneppen, Radoslaw Wojtak, Liliya Williams, Claudia Scarlata, Vasily Kokorev, Gabriel Brammer, Bahram Mobasher, Jose Maria Diego, John Weaver, Mike Boylan-Kolchin, Amanda Pagul, Christian Jespersen, Anna Niemiec and Ana Acebron Munoz.

Lastly, I would like to thank my previous supervisors Peter G. Martin and Antoine Marchal, without whom I never would have gotten my first research experience. I am eternally indebted to them for giving me the opportunity to get my foot in the door, and pursue a career in the field that I have always loved.

References

Allen, S. W., Evrard, A. E., & Mantz, A. B. 2011, , 49, 409, doi: 10.1146/annurev-astro-081710-102514

Barkana, R., & Loeb, A. 2001, Physics Reports, 349, 125, doi: 10.1016/s0370-1573(01)00019-9

Bartelmann, M., & Schneider, P. 2001, Physics Reports, 340, 291, doi: 10.1016/s0370-1573(00)00082-x

Behroozi, P., & Silk, J. 2018, Monthly Notices of the Royal Astronomical Society, 477, 5382, doi: 10.1093/mnras/sty945

Bond, J. R., Cole, S., Efstathiou, G., & Kaiser, N. 1991, , 379, 440, doi: 10.1086/170520

Bouwens, R., Illingworth, G., Oesch, P., et al. 2023, Monthly Notices of the Royal Astronomical Society, doi: 10.1093/mnras/stad1014

Bouwens, R. J., Illingworth, G. D., Oesch, P. A., et al. 2015, The Astrophysical Journal, 803, 34, doi: 10.1088/0004-637x/803/1/34

Boylan-Kolchin, M. 2023a, Nature Astronomy, doi: 10.1038/s41550-023-01937-7

—. 2023b, Nature Astronomy, doi: 10.1038/s41550-023-01937-7

Broadhurst, T., Takada, M., Umetsu, K., et al. 2005, The Astrophysical Journal, 619, L143, doi: 10.1086/428122

Bromm, V., Coppi, P. S., & Larson, R. B. 2002, The Astrophysical Journal, 564, 23, doi: 10.1086/323947

Bromm, V., & Yoshida, N. 2011, Annual Review of Astronomy and Astrophysics, 49, 373, doi: 10.1146/annurev-astro-081710-102608

Bulbul, E., Chiu, I. N., Mohr, J. J., et al. 2019, , 871, 50, doi: 10.3847/1538-4357/aaf230

Caminha, G. B., Suyu, S. H., Grillo, C., & Rosati, P. 2022, Astronomy &amp Astrophysics, 657, A83, doi: 10.1051/0004-6361/202141994

Clowe, D., Bradač, M., Gonzalez, A. H., et al. 2006, The Astrophysical Journal, 648, L109, doi: 10.1086/508162

Clowe, D., Gonzalez, A., & Markevitch, M. 2004, The Astrophysical Journal, 604, 596, doi: 10.1086/381970

Desjacques, V., Jeong, D., & Schmidt, F. 2018, Physics Reports, 733, 1, doi: 10.1016/j.physrep.2017.12.002

Diego, J. M., Pascale, M., Kavanagh, B. J., et al. 2022, Astronomy &amp Astrophysics, 665, A134, doi: 10.1051/0004-6361/202243605

Diego, J. M., Protopapas, P., Sandvik, H. B., & Tegmark, M. 2005, Monthly Notices of the Royal Astronomical Society, 360, 477, doi: 10.1111/j.1365-2966.2005.09021.x

Diego, J. M., Tegmark, M., Protopapas, P., & Sandvik, H. B. 2007, Monthly Notices of the Royal Astronomical Society, 375, 958, doi: 10.1111/j.1365-2966.2007.11380.x

Diego, J. M., Broadhurst, T., Chen, C., et al. 2015, Monthly Notices of the Royal Astronomical Society, 456, 356, doi: 10.1093/mnras/stv2638

Diego, J. M., Meena, A. K., Adams, N. J., et al. 2023, Astronomy &amp Astrophysics, 672, A3, doi: 10.1051/0004-6361/202245238

Diemer, B., & Kravtsov, A. V. 2015, , 799, 108, doi: 10.1088/0004-637X/799/1/108

Donnan, C. T., McLeod, D. J., Dunlop, J. S., et al. 2022, Monthly Notices of the Royal Astronomical Society, 518, 6011, doi: 10.1093/mnras/stac3472

Dyson, F. W., Eddington, A. S., & Davidson, C. 1920, Philosophical Transactions of the Royal Society of London Series A, 220, 291, doi: 10.1098/rsta.1920.0009

Ezquiaga, J. M., García-Bellido, J., & Vennin, V. 2023, Massive galaxy clusters like "El Gordo" hint at primordial quantum diffusion. https://arxiv.org/abs/2207.06317

Finkelstein, S. L., Song, M., Behroozi, P., et al. 2015, , 814, 95, doi: 10.1088/0004-637X/814/2/95

Finkelstein, S. L., Bagley, M. B., Ferguson, H. C., et al. 2022, arXiv e-prints, arXiv:2211.05792, doi: 10.48550/arXiv.2211.05792

Finkelstein, S. L., Bagley, M. B., Ferguson, H. C., et al. 2023, The Astrophysical Journal Letters, 946, L13, doi: 10.3847/2041-8213/acade4

Ghosh, A., Williams, L. L. R., Liesenborgs, J., et al. 2021, , 506, 6144, doi: 10.1093/mnras/stab1196

Glazebrook, K., Schreiber, C., Labbé, I., et al. 2017, , 544, 71, doi: 10.1038/nature21680

Haiman, Z., Rees, M. J., & Loeb, A. 1997, The Astrophysical Journal, 476, 458, doi: 10.1086/303647

Harikane, Y., Ouchi, M., Oguri, M., et al. 2023, The Astrophysical Journal Supplement Series, 265, 5, doi: 10.3847/1538-4365/acaaa9

Haro, P. A., Dickinson, M., Finkelstein, S. L., et al. 2023, Spectroscopic verification of very luminous galaxy candidates in the early universe. https://arxiv.org/abs/2303.15431

Haslam, C. G. T., Large, M. I., & Quigley, M. J. S. 1964, , 127, 273, doi: 10.1093/mnras/127.4.273

Jauzac, M., Harvey, D., & Massey, R. 2018, Monthly Notices of the Royal Astronomical Society, 477, 4046, doi: 10.1093/mnras/sty909

Jenkins, A., Frenk, C. S., White, S. D. M., et al. 2001, Monthly Notices of the Royal Astronomical Society, 321, 372, doi: 10.1046/j.1365-8711.2001.04029.x

Johnson, T. L., Sharon, K., Bayliss, M. B., et al. 2014, , 797, 48, doi: 10.1088/0004-637X/797/1/48

Jullo, E., & Kneib, J. P. 2009, , 395, 1319, doi: 10.1111/j.1365-2966.2009.14654.x

Jullo, E., Kneib, J. P., Limousin, M., et al. 2007, New Journal of Physics, 9, 447, doi: 10.1088/1367-2630/9/12/447

Kneib, J. P., Ellis, R. S., Smail, I., Couch, W. J., & Sharples, R. M. 1996, , 471, 643, doi: 10.1086/177995

Labbé, I., van Dokkum, P., Nelson, E., et al. 2023, Nature, 616, 266, doi: 10.1038/s41586-023-05786-2

Lacey, C. G., Baugh, C. M., Frenk, C. S., & Benson, A. J. 2011, Monthly Notices of the Royal Astronomical Society, 412, 1828, doi: 10.1111/j.1365-2966.2010.18021.x

Limousin, M., Beauchesne, B., & Jullo, E. 2022, Astronomy &amp Astrophysics, 664, A90, doi: 10.1051/0004-6361/202243278

Lotz, J. M., Koekemoer, A., Coe, D., et al. 2017, The Astrophysical Journal, 837, 97, doi: 10.3847/1538-4357/837/1/97

Lovisari, L., & Maughan, B. J. 2022, in Handbook of X-ray and Gamma-ray Astrophysics (Springer Nature Singapore), 1–50, doi: 10.1007/978-981-16-4544-0_118-1

Lubin, L. M., Cen, R., Bahcall, N. A., & Ostriker, J. P. 1996, , 460, 10, doi: 10.1086/176948

Lukić , Z., Heitmann, K., Habib, S., Bashinsky, S., & Ricker, P. M. 2007, The Astrophysical Journal, 671, 1160, doi: 10.1086/523083

Moster, B. P., Somerville, R. S., Newman, J. A., & Rix, H.-W. 2011, The Astrophysical Journal, 731, 113, doi: 10.1088/0004-637x/731/2/113

Murray, S., Power, C., & Robotham, A. 2013, HMFcalc: An Online Tool for Calculating Dark Matter Halo Mass Functions. https://arxiv.org/abs/1306.6721

Naidu, R. P., Oesch, P. A., Setton, D. J., et al. 2022, Schrodinger's Galaxy Candidate: Puzzlingly Luminous at $z \approx 17$, or Dusty/Quenched at $z \approx 5$? https://arxiv.org/abs/2208.02794

Narayan, R., & Bartelmann, M. 1997, Lectures on Gravitational Lensing. https://arxiv.org/abs/astro-ph/9606001

Navarro, J. F., Frenk, C. S., & White, S. D. M. 1997, , 490, 493, doi: 10.1086/304888

Newman, J. A., & Davis, M. 2002, The Astrophysical Journal, 564, 567, doi: 10.1086/324148

Newton, I. 1704, Opticks (Dover Press)

Peebles, P. J. E. 1980, The large-scale structure of the universe

Postman, M., Coe, D., Benítez, N., et al. 2012, The Astrophysical Journal Supplement Series, 199, 25, doi: 10.1088/0067-0049/199/2/25

Press, W. H., & Schechter, P. 1974, , 187, 425, doi: 10.1086/152650

Richard, J., Claeyssens, A., Lagattuta, D., et al. 2021, Astronomy &amp Astrophysics, 646, A83, doi: 10.1051/0004-6361/202039462

Robertson, B. E., Tacchella, S., Johnson, B. D., et al. 2022, Discovery and properties of the earliest galaxies with confirmed distances. https://arxiv.org/abs/2212.04480

Sendra, I., Diego, J. M., Broadhurst, T., & Lazkoz, R. 2013, Monthly Notices of the Royal Astronomical Society, 437, 2642, doi: 10.1093/mnras/stt2076

Sheth, R. K., Mo, H. J., & Tormen, G. 2001, Monthly Notices of the Royal Astronomical Society, 323, 1, doi: 10.1046/j.1365-8711.2001.04006.x

Song, M., Finkelstein, S. L., Ashby, M. L. N., et al. 2016, The Astrophysical Journal, 825, 5, doi: 10.3847/0004-637x/825/1/5

Springel, V., White, S. D. M., Jenkins, A., et al. 2005, Nature, 435, 629, doi: 10.1038/nature03597

Steinhardt, C. L., Capak, P., Masters, D., & Speagle, J. S. 2016, The Astrophysical Journal, 824, 21, doi: 10.3847/0004-637x/824/1/21

Steinhardt, C. L., Jespersen, C. K., & Linzer, N. B. 2021, The Astrophysical Journal, 923, 8, doi: 10.3847/1538-4357/ac2a2f

Steinhardt, C. L., Kokorev, V., Rusakov, V., Garcia, E., & Sneppen, A. 2022, Templates for Fitting Photometry of Ultra-High-Redshift Galaxies. https://arxiv.org/abs/2208.07879

Steinhardt, C. L., Jauzac, M., Acebron, A., et al. 2020, The Astrophysical Journal Supplement Series, 247, 64, doi: 10.3847/1538-4365/ab75ed

Vikhlinin, A., Kravtsov, A. V., Burenin, R. A., et al. 2009, , 692, 1060, doi: 10.1088/0004-637X/692/2/1060

Visbal, E., Barkana, R., Fialkov, A., Tseliakhovich, D., & Hirata, C. M. 2012, Nature, 487, 70, doi: 10.1038/nature11177

Visbal, E., Haiman, Z., & Bryan, G. L. 2018, Monthly Notices of the Royal Astronomical Society, 475, 5246, doi: 10.1093/mnras/sty142

Vogelsberger, M., Genel, S., Springel, V., et al. 2014, , 509, 177, doi: 10.1038/nature13316

White, D. A., & Fabian, A. C. 1995, , 273, 72, doi: 10.1093/mnras/273.1.72

White, S. D. M., Navarro, J. F., Evrard, A. E., & Frenk, C. S. 1993, , 366, 429, doi: 10.1038/366429a0

Wright, C. O., & Brainerd, T. G. 1999, Gravitational Lensing by NFW Halos. https://arxiv.org/abs/astro-ph/9908213

Yung, L. Y. A., Somerville, R. S., Finkelstein, S. L., Wilkins, S. M., & Gardner, J. P. 2023, arXiv e-prints, arXiv:2304.04348, doi: 10.48550/arXiv.2304.04348

Zavala, J., & Frenk, C. S. 2019, Dark matter haloes and subhaloes. https://arxiv.org/abs/1907.11775

Zavala, J. A., Buat, V., Casey, C. M., et al. 2023, , 943, L9, doi: 10.3847/2041-8213/acacfe

Zhao, D. H., Jing, Y. P., Mo, H. J., & Börner, G. 2009, The Astrophysical Journal, 707, 354, doi: 10.1088/0004-637x/707/1/354

Zhao, D. H., Mo, H. J., Jing, Y. P., & Börner, G. 2003, , 339, 12, doi: 10.1046/j.1365-8711.2003.06135.x

Zitrin, A., Broadhurst, T., Umetsu, K., et al. 2009, Monthly Notices of the Royal Astronomical Society, 396, 1985, doi: 10.1111/j.1365-2966.2009.14899.x

Zitrin, A., Fabris, A., Merten, J., et al. 2015, , 801, 44, doi: 10.1088/0004-637X/801/1/44

Zitrin, A., Labbé , I., Belli, S., et al. 2015, The Astrophysical Journal, 810, L12, doi: 10.1088/2041-8205/810/1/l12